machines

MDPI

Article

Hollow-Type Integrated Assembly Design and Performance Validation of Conductive Slip Rings via Simulation-Driven Optimization

Zhiyuan Qian [1], Chao Han [2], Nianhuan Li [2], Gongqiang Tian [2], Junye Li [2,*] and Haihong Wu [3]

[1] National Key Laboratory of Aerospace Mechanism, Aerospace System Engineering Shanghai, Shanghai 201108, China; qzy0024@163.com
[2] School of Mechatronic Engineering, Changchun University of Science and Technology, Changchun 130012, China; 18263302088@163.com (C.H.); m15844087816@163.com (N.L.); ccst3022@163.com (G.T.)
[3] China Shipbuilding Jiujiang Marine Equipment (Group) Co., Ltd., Jiujiang 332000, China; lnhlxy@163.com
* Correspondence: ljy@cust.edu.cn; Tel.: +86-136-4430-2228

Abstract: Conductive slip rings (CSRs) are precision components critical to industrial equipment, yet they face challenges such as unstable signal transmission, limited functionality, and difficulties in operational monitoring due to assembly-induced inaccuracies. This study proposes a hollow-type integrated assembly solution, incorporating optimized transmission, clamping, and protection modules through structural design and modular analysis. Static and dynamic simulations identify the optimal assembly angle and connector configuration (hollow-type outperforming flange-type), ensuring reliability and stability. A high-precision universal assembly platform is designed, and an R-axis rotary table-based testing method is developed to evaluate transmission and fixation modes. Results demonstrate the superiority of sleeve couplings and hollow connectors, with the assembled system achieving contact resistance fluctuations below 10 mΩ, angular repeatability under 500″, and accuracy within 720″, meeting all design specifications. The proposed framework combines simulation-driven design with experimental validation, offering a robust approach to enhance the performance of CSRs in industrial applications.

Keywords: conductive slip ring; hollow integrated assembly; static/dynamic simulation; performance testing

check for updates

Academic Editor: Luca Bruzzone

Received: 17 April 2025
Revised: 10 May 2025
Accepted: 12 May 2025
Published: 15 May 2025

Citation: Qian, Z.; Han, C.; Li, N.; Tian, G.; Li, J.; Wu, H. Hollow-Type Integrated Assembly Design and Performance Validation of Conductive Slip Rings via Simulation-Driven Optimization. *Machines* **2025**, *13*, 415. https://doi.org/10.3390/machines13050415

Copyright: © 2025 by the authors. Licensee MDPI, Basel, Switzerland. This article is an open access article distributed under the terms and conditions of the Creative Commons Attribution (CC BY) license (https://creativecommons.org/licenses/by/4.0/).

1. Introduction

The conductive slip ring (CSR), also known as a collector ring or rotating joint, is a precision device for signal and power transmission between rotating mechanisms. It is widely used in aerospace, maritime, defense, and robotics [1]. In aerospace, it supports aircraft navigation, communication, and operation systems. In maritime applications, it monitors ship status and performance. In defense, it plays a critical role in missile systems and armored vehicles. With the growth of industrial automation and robotics, slip rings have become core components in robotics, driving a significant rise in market demand. It is projected that the global market will reach USD 1.1 billion by 2030 [2].

Encoders convert motion displacement into electrical signals to determine parameters like angle and position, playing a significant role in industrial applications. Common types include optical and magnetic encoders. Optical encoders use grating diffraction principles for angle detection, offering compact structure and long lifespan [3]. Magnetic encoders

rely on the Hall effect for angle detection and are known for their small size, light weight, and ease of operation [4].

As industrial equipment becomes more compact, the demand for accurate positioning technologies increases. Electrical slip rings face challenges such as signal instability and limited functionality. Combining them with encoders into an integrated assembly structure addresses these issues, improving system reliability and stability and ensuring the safe operation of the slip rings.

Research on CSRs has mainly focused on the modification and optimization of the internal structures. For instance, Niu G et al. proposed a predictive model for brushless CSRs that better reflects the actual wear process and guides the optimization of design parameters [4]. Shumin Z et al. studied the tribological properties of alloy rings and brushes, finding that increasing the hardness of the ring can reduce the friction coefficient and wear rate [5]. Li J et al. proposed a machine vision-based method for measuring and controlling brush wire angles that demonstrated small measurement errors [6]. Chen X et al. developed a vision-assisted brush wire alignment assembly system, improving alignment accuracy and efficiency [7]. Furthermore, scholars such as Jia Qingjian have studied the variation in the friction torque of slip rings under different environmental conditions [8]. Yang Jingyao et al. used numerical analysis methods to study the heat transfer characteristics of brush-sealed systems [9]. Jiang Kai et al. designed a CSR wiring structure for underwater miniature submersibles [10]. Li Wenguo et al. developed a new type of ultra-small CSR [11]. Li Wenguo et al. emphasized the critical role of centroid balancing in extending the service life of CSRs [12]. Liu Ming et al. analyzed the working principle and dynamics of the "gooseneck"-type slip ring [13]. However, there is relatively little research on the modification of the external structure and assembly of CSRs both domestically and internationally.

Research in the field of encoders has also yielded significant results. Feng T et al. proposed a new magnetic encoder structure to improve accuracy and magnetic field coverage and introduced a specialized decoding algorithm [14]. Wang S et al. proposed an effective temperature compensation method based on a backpropagation neural network [15]. Han S et al. developed a multi-resolution encoder and validated its performance [16]. Sun Z et al. proposed a sequence encoder for identity verification [17]. Furthermore, Zhang Bo et al. designed a high-precision magnetoelectric rotary encoder and tested it [18]. Wang Chengfeng et al. improved the mounting structure of the speed encoder [19]. Huang Lixia et al. proposed the use of new high-performance giant magnetoresistance sensors [20]. Yin Qingyan et al. proposed a survival analysis algorithm based on multi-omics data and sparse variational autoencoders [21]. Sheng Didi optimized the DBN for compensating magnetic encoding errors based on the PSO algorithm [22]. Zhao Ruofei designed a high-bit, high-precision magnetic encoder based on tunneling magnetoresistance technology [23]. Overall, encoder research has predominantly focused on internal structure optimization, with relatively little attention given to external structure modification and assembly research.

In the field of structural assembly, both domestic and international scholars have also conducted extensive research. Ludois D C et al. proposed a rotary electrochemical double-layer capacitor and related innovative designs [24]. Domestic scholars, such as Tu Wenying et al., analyzed the causes of spindle system errors and implemented technical measures to reduce assembly errors [25]. Wang Yaoyu discussed the standard connection methods for motors and encoders, as well as assembly considerations [26]. Research on CSRs has primarily focused on internal structural modifications and optimizations, such as predictive models for brushless CSRs, tribological property studies, and machine vision-based methods for brush wire angle measurement and control. However, there

is limited research on external structural modifications and the assembly of CSRs both domestically and internationally. Similarly, encoder research has mainly concentrated on internal structure optimization, with relatively little attention given to external structure modification and assembly.

Based on the current state of research, this paper focuses on the integrated assembly of CSRs and encoders. Through finite element analysis and experimental methods, this study comprehensively analyzes the factors affecting the reliability, stability, and operational accuracy of the assembly, aiming to address the challenges in the monitoring and failure of CSRs in industrial equipment and to achieve integrated assembly of the slip ring and encoder. Through finite element analysis and experimental methods, this study comprehensively analyzes the factors affecting the reliability, stability, and operational accuracy of the assembly, aiming to address the challenges in the monitoring and failure of CSRs in industrial equipment and to achieve integrated assembly of the slip ring and encoder. The specific research tasks are as follows:

(1) Overall design of the hollow assembly. Based on the structural characteristics of the CSR and encoder, the overall design approach is clarified and the working principle analyzed. The design covers aspects such as the selection of the drive, clamping, protection, and instrumentation modules. Through subsequent simulations and experiments, the performance of the assembly is validated and the versatility of the encoder in two different slip ring structures is assessed.

(2) Using finite element analysis, study the static and dynamic characteristics of the hollow assembly. The static and dynamic characteristics are analyzed in depth. Static characteristic simulations are conducted for different assembly angles of the hollow connection frame in the hollow assembly to determine the optimal assembly configuration. On this basis, further static and dynamic characteristic simulations are performed to obtain key parameters such as stress, displacement, and natural frequencies. The overall modal simulation results of the hollow connection frame and flange-type connection frame are compared to identify the optimal assembly structure.

(3) Design an assembly platform, including calibration of the rotating platform and the design of the support, protection, and digital display modules. Based on this platform, a performance testing device for the hollow assembly is constructed to analyze the sources of assembly errors and their theoretical foundations. A performance testing method is proposed based on the R-axis rotating platform. Contact resistance testing is carried out on the hollow assembly to investigate the influence of different transmission and fixation methods on testing accuracy and determine the optimal transmission and fixation structures. Based on this, angle repeatability and precision testing experiments are conducted to ensure the assembly meets the technical specifications.

2. Hollow Assembly of CSRs

2.1. Overall Design

The hollow assembly of the CSR has an integrated structural design (see Figures 1 and 2) consisting of four main functional units: the drive module, clamping module, protection module, and instrumentation module.

In the horizontally placed configuration, the composition and function of each module are as follows:

1. Drive Module: Combines the optical shaft drive with a sleeve-type coupling for power transmission;
2. Clamping Module: Fixes the through-hole slip ring and optoelectronic encoder via the hollow connector frame, providing structural support;

3. Protection Module: Includes the small-hole adapter plate and the guide sleeve-type protective cover. The former is fixed to the connector frame, and the latter provides protective integration with the slip ring and encoder;
4. Instrumentation Module: Integrates the through-hole slip ring and optoelectronic encoder, with the encoder's rotating shaft directly connected to the coupling of the drive module.

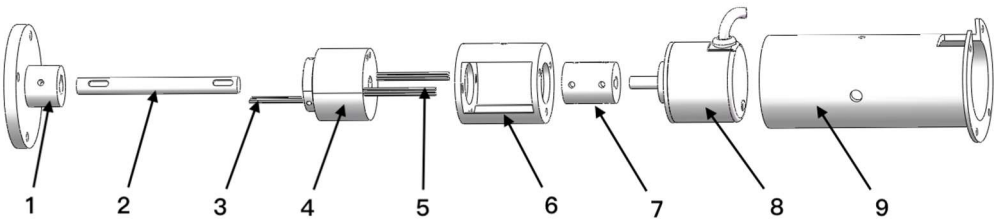


Figure 1. Exploded view of the hollow assembly. 1—Small-hole adapter plate; 2—Optical shaft drive; 3—Through-hole slip ring rotor lead; 4—Through-hole slip ring; 5—Through-hole slip ring stator lead; 6—Hollow connector frame; 7—Sleeve-type coupling; 8—Optoelectronic encoder; 9—Guide sleeve-type protective cover.

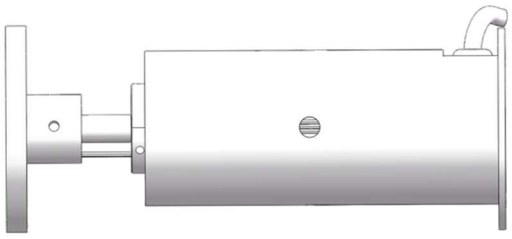


Figure 2. Three-dimensional model of the hollow assembly.

The following section will provide a detailed explanation of the design and selection schemes for each module when in the horizontally placed configuration.

2.2. Design of the Drive Module

As the actuator of the hollow assembly, the design scheme of the drive module needs to be optimized among pneumatic, hydraulic, electromagnetic, and mechanical transmission systems. Based on the features of simple rotational motion of the assembly, compact and integrated structural constraints, and the need for transmission stability and reliability, the mechanical transmission solution is ultimately selected (see Figure 3 for the specific structure).

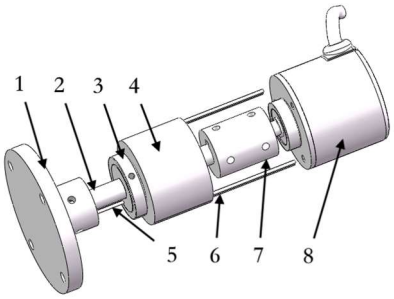


Figure 3. Three-dimensional model of the hollow assembly drive module. 1—Small-hole adapter plate; 2—Optical shaft drive; 3—Through-hole slip ring rotor; 4—Through-hole slip ring stator; 5—Through-hole slip ring rotor lead; 6—Through-hole slip ring stator lead; 7—Sleeve-type coupling; 8—Optoelectronic encoder.

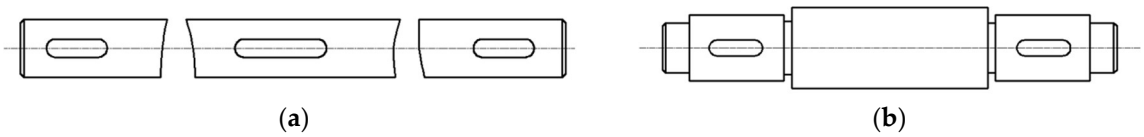
This module adopts a layered transmission architecture:

1. Drive Layer: The small-hole adapter plate serves as the power input;
2. Transmission Layer: Composed of the optical shaft drive, through-hole slip ring rotor, and sleeve-type coupling to form the motion transmission chain;
3. Detection Layer: The optoelectronic encoder is directly connected via the coupling to receive rotational signal data.

During operation, the mechanical transmission chain converts the rotational motion of the adapter plate through three transmission components, ultimately transforming it into the precise angular displacement output of the optoelectronic encoder's rotating shaft.

2.2.1. Design of the Optical Shaft Drive

To achieve synchronous rotation between the small-hole adapter plate and the through-hole slip ring rotor, a through-type solid shaft is required. Comparing the characteristics of optical shafts and stepped shafts shown in Figure 4, optical shafts have lower processing costs but poor axial positioning, while stepped shafts achieve precise positioning through shoulder features. Considering the radial load dominance of the assembly and the need to simplify the processing complexity, the optical shaft is ultimately selected as the base structure of the drive shaft.



(**a**) (**b**)

Figure 4. Solid shaft structure diagram. (**a**) Optical shaft; (**b**) stepped shaft.

As shown in Figure 5, the optical shaft drive adopts an integrated design, serving both torque transmission and rotational support functions. Its connection structure includes three key interfaces:

1. Slip Ring Interface: The shaft and slip ring rotor are fitted using an H7/k6 transition fit. Radially distributed threaded holes with three radial set screws achieve circumferential locking, ensuring synchronization accuracy;
2. Adapter Plate Interface: The shaft end features a standard keyway, with an A-type flat key forming a shear-resistant transmission fit with the small-hole adapter plate;
3. Coupling Interface: The symmetric ends are equipped with identical keyway structures, establishing a torque transmission path with equal strength to the sleeve-type coupling.

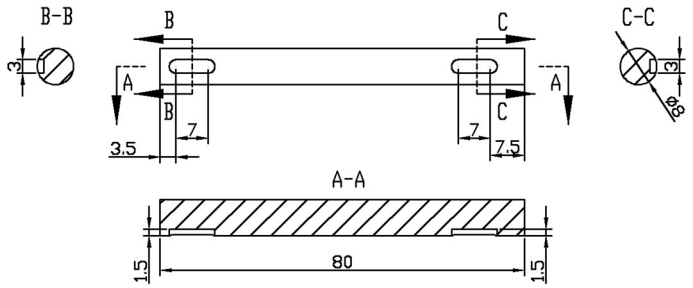


Figure 5. Schematic design of an optical shaft drive shaft.

Based on the inherent dimensions of the through-hole slip ring rotor, the inner hole design of the small-hole adapter plate, and the inner hole design of the sleeve-type coupling, the hole diameter of the through-hole slip ring rotor is 8 mm, the inner hole diameter of the small-hole adapter plate is 8 mm, and the inner hole diameter of the sleeve-type coupling is also 8 mm. To avoid excessive steps on the optical shaft drive, which may cause uneven

loading and to facilitate assembly, the total length of the optical shaft drive is set to 80 mm, with a shaft diameter of 8 mm. As a transmission component, the optical shaft drive needs to withstand a certain amount of torque. Therefore, the chosen material must minimize the impact of torsional deformation. Ultimately, 45 steel, which has a yield strength of 355 MPa, is selected as the material for the optical shaft drive.

The optical shaft drive is a solid shaft with a known length and diameter, so its section polar moment of inertia I_{p2} can be calculated:

$$I_{p2} = \int_0^{2\pi} \int_0^{R_2} \rho^3 d\rho d\theta = \frac{\pi D_2^4}{32}, \tag{1}$$

where D_2 is the diameter of the circular cross section, from which the torsional section modulus W_{t2} can be calculated:

$$W_{t2} = \frac{I_{p2}}{R_2} = \frac{\pi D_2^3}{16}, \tag{2}$$

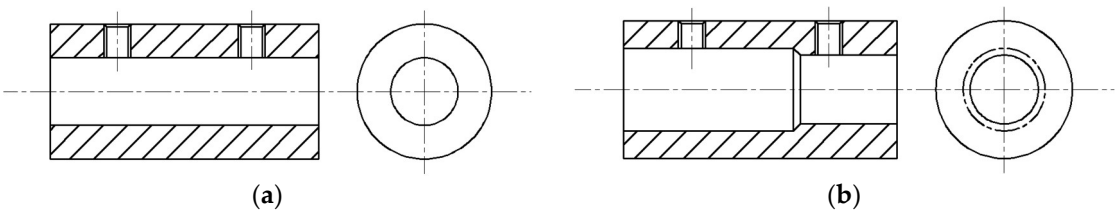
where R_2 is the radius of the circular cross section. When the light shaft drive shaft rotates, its maximum shear stress $\tau_{2\max}$ should not exceed the allowable stress $[\tau]$:

$$W_{t2} = \frac{I_{p2}}{R_2} = \frac{\pi D_2^3}{16}, \tag{3}$$

Based on the torque characteristics of the closed-hole slip ring and optical encoder, as well as the driving torque of common small motors, the maximum torque $T_{3\max}$ for the hollow assembly is set to 3 N·m. From Equations (1)–(3), the maximum shear stress of the light shaft drive shaft is calculated to be 29.842 MPa, which is well below the allowable stress of the material. Therefore, the material selection and dimensional parameters of the light shaft drive shaft meet the torsional strength requirements of the hollow assembly.

2.2.2. Design of the Sleeve Coupling

To achieve synchronized rotation and torque transmission between the small-hole adapter plate and the optical encoder's rotating shaft, an integrated coupling is required for connection. The integrated coupling is mainly divided into two types: light-hole couplings and stepped-hole couplings (as shown in Figure 6). The light-hole coupling has a through hole inside and fixes the shaft with a set screw, primarily bearing radial forces, whereas the stepped-hole coupling has varying diameters at different cross sections, providing better axial positioning capability. It is important to note that the standard integrated coupling is a rigid coupling lacking displacement compensation ability and thus unable to effectively eliminate vibrations and shocks. If an annular channel is introduced on its side, it can be transformed into a flexible coupling, which would provide displacement compensation and vibration-damping capabilities.



(**a**) (**b**)

Figure 6. Schematic diagram of integrated coupling structure. (**a**) Integrated light-hole coupling; (**b**) integrated stepped-hole coupling.

Considering the compact and integrated structure of the hollow assembly and the characteristics of medium-to-low speed transmission, a rigid integrated stepped-hole coupling is chosen as the sleeve coupling in this study. The sleeve coupling serves as a key connecting component between the light-shaft drive shaft and the optical encoder's rotating shaft, transmitting torque and also providing axial positioning. The coupling features a central round hole and keyway at both the large and small hole ends, with three threaded holes distributed on the left, right, and upper sides, all centered on the hole center. The central round hole at the large hole end connects to the light-shaft drive shaft, while the small hole end connects to the optical encoder's rotating shaft. Torque transmission is achieved through a combination of flat keys and set screws at both ends (as shown in Figure 7). Based on the above selection criteria, this study presents the structural design of the sleeve coupling [27–29].

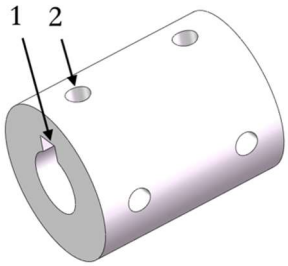


Figure 7. Three-dimensional model of sleeve coupling. 1—Keyway; 2—Threaded hole.

As a rotating component, the sleeve coupling bears a certain torque during operation and undergoes torsional deformation. Studying the stress and deformation characteristics of the sleeve coupling under torque is crucial to ensure the reliability of the hollow assembly.

Figure 8 shows the von Mises stress and displacement simulation maps of the sleeve coupling under a 3 N·m torque. The analysis results show that the maximum stress is 31.8 MPa, located at the edge of the central hole where it connects to the light-shaft drive shaft, with other areas experiencing stress levels mostly below 15 MPa. The maximum deformation displacement is 0.227 µm, occurring at the edge of the central hole and the corresponding outer circular edge. In summary, the stress and deformation of the sleeve coupling under torque are minimal, allowing it to maintain a close fit with the light-shaft drive shaft contact surface and preventing excessive deformation, thereby ensuring the operational reliability of the hollow assembly.

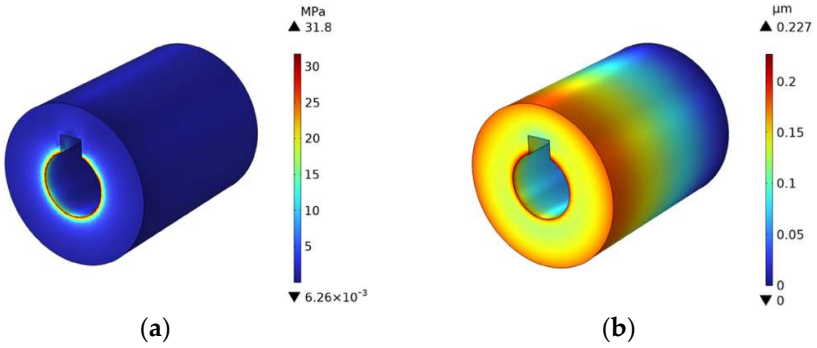


Figure 8. Simulation maps of von Mises stress and displacement for the sleeve coupling. (**a**) Von Mises stress map; (**b**) displacement map.

2.3. Design of the Clamping Module

The clamping module, as the core fixation mechanism of the hollow assembly, must meet the compatibility assembly requirements between the through-hole slip ring and

various optical encoders. This study focuses on general-purpose through-hole slip rings and mainstream optical encoders and proposes an innovative modular clamping system. For the special assembly requirements of the same type of hollow optical encoder, precise connection is achieved through the use of an auxiliary short shaft. Based on the technical specifications, working environment, and installation requirements of the assembly, the clamping module system shown in Figure 9 was ultimately developed.

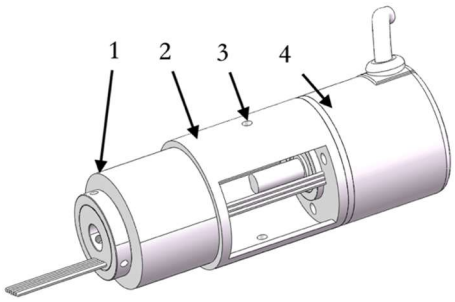


Figure 9. Three-dimensional model of the clamping module for hollow assembly. 1—Through-hole slip ring; 2—Hollow connection frame; 3—Side-threaded holes of the hollow connection frame; 4—Optical encoder.

The clamping module mainly consists of three components: the through-hole slip ring, hollow connection frame, and optical encoder (as shown in Figure 10). The system uses the through-hole slip ring stator and hollow connection frame as fixed components to achieve stable fixation of the non-rotating part of the optical encoder. Based on the structural analysis of the through-hole slip ring and mainstream optical encoders, two innovative connection frame fixation structures were designed: hollow and flange types.

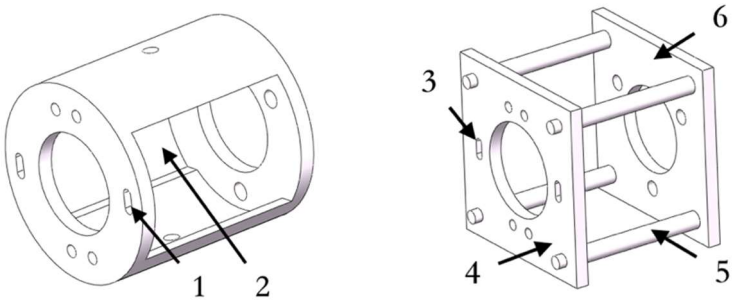


Figure 10. Three-dimensional model of the hollow and flange connection frames. 1—Hollow connection frame wiring straight slot; 2—Hollow connection frame wiring hole; 3—Flange connection frame wiring straight slot; 4—Through-hole slip ring flange; 5—Fixed connection rod; 6—Optical encoder flange.

Both types of connection frames have two circular through-holes on the top and bottom contact surfaces at the through-hole slip ring end, with two straight slots on each side and a central hole in the middle. The four through-holes are connected by screws to ensure a firm connection between the fixed end of the through-hole slip ring and the connection frame. The two straight slots allow the wiring of the slip ring stator to pass through the through-holes, while the central hole provides the necessary space for the rotation of the slip ring rotor. On the optical encoder end contact surface, both connection frames evenly distribute three through-holes and one central hole: the three through-holes are connected by screws to ensure a reliable fixation of the optical encoder to the connection frame, while the central hole provides a channel for the connection between the sleeve coupling and the optical encoder, ensuring a precise fit with the encoder's protruding parts to meet the coaxiality requirements.

The hollow connection frame features two threaded holes on both side ends and wiring holes on the other two sides. The two threaded holes are used for connecting the guide sleeve-type fixing cover, and the wiring holes provide a dedicated channel for the wiring of the through-hole slip ring stator. The flange connection frame adopts a fixed connection rod design, which provides more space for wiring but is not suitable for mounting the guide sleeve-type fixing cover.

2.4. Design of the Protection Module

2.4.1. Design of the Small Hole Type Adapter Plate

During operation, the hollow assembly must transfer power to the rotating device. Direct connection to the light-shaft transmission shaft may result in insufficient structural strength, increasing the risk of failure (as shown in Figure 11). To address this, this study proposes a transition connection mechanism by introducing a small-hole-type adapter plate as the core transmission component, achieving both power transmission and safety protection while ensuring assembly accuracy.

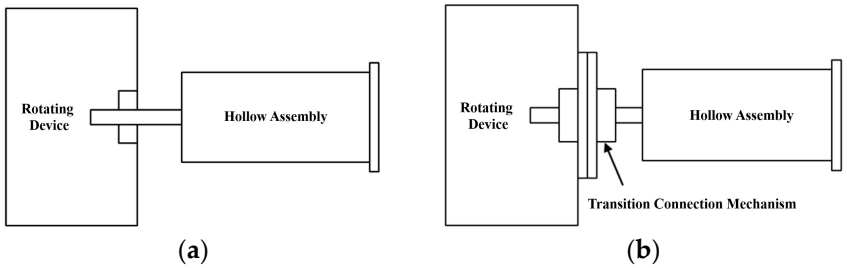


Figure 11. Schematic diagram of the hollow assembly connecting to the rotating device. (**a**) Direct connection; (**b**) indirect connection.

The small-hole-type adapter plate is a key transition element between the light-shaft transmission shaft and the rotating device, serving both torque transmission and axial support functions. The adapter plate uses a symmetric design with a large disk at one end containing four evenly distributed through-holes for connecting to the rotating device (Figure 12). The through-holes use threaded fittings for circumferential fixation, while the end boss is designed with a keyed inner hole structure. The combination of a flat key and a set screw ensures precise connection to the light-shaft transmission shaft. Based on the torque transmission characteristics and structural strength requirements, this paper presents the parametric design of the small-hole-type adapter plate shown in Figure 12.

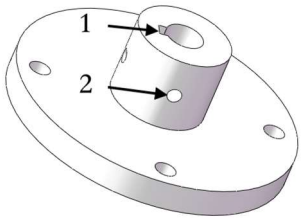
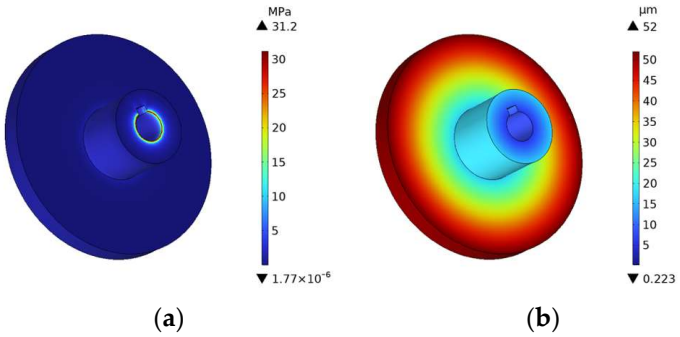


Figure 12. Three-dimensional model of the small-hole-type adapter plate. 1—Keyway; 2—Threaded hole.

As the core load-bearing component of the rotating system, the small-hole-type adapter plate undergoes complex stress under working conditions. Analyzing its mechanical response under rated load is crucial for verifying the reliability of the assembly.

Finite element simulation was used to analyze the stress distribution characteristics of the adapter plate under a 3 N·m torque (Figure 13). The analysis shows that a maximum equivalent stress of 31.2 MPa occurs at the edge of the transmission shaft connection hole, which is below the material's yield strength. The stress distribution in other areas is

relatively uniform, with the maximum value not exceeding 15 MPa. Deformation analysis shows that the maximum displacement of 52 μm occurs at the edge of the rotating drive end, meeting the micron-level assembly precision requirements. The simulation results validate the structural integrity of the adapter plate under dynamic conditions, with stress levels within the safety threshold, effectively ensuring the operational stability of the hollow assembly.



(**a**) (**b**)

Figure 13. Von Mises stress and displacement simulation results for the small-hole-type adapter plate. (**a**) Von Mises stress map; (**b**) displacement map.

2.4.2. Design of the Guide Sleeve Type Fixed Cover

To meet the environmental adaptability requirements of the hollow assembly under complex working conditions, this study proposes the guide-sleeve fixed cover as a key protective component (Figure 14). The device, with its multi-dimensional protective design, effectively isolates temperature and humidity fluctuations, dust contamination, and foreign object intrusion, significantly enhancing the system's operational reliability in harsh environments.

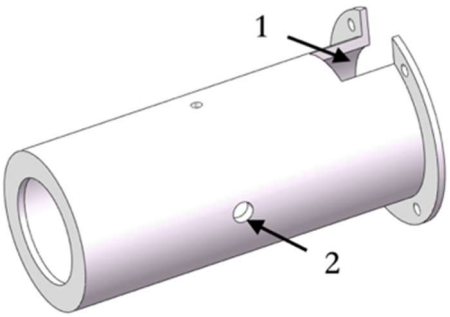


Figure 14. Three-dimensional model of the guide-sleeve fixed cover. 1—Optical encoder wiring hole; 2—Through-hole slip ring wiring hole.

Based on the analysis of the interface characteristics between the transmission and clamping modules, an innovative guide-sleeve fixed cover structure with composite protection functions was designed. The main technical features of this component are:

1. Dynamic connection channel: The central hole on the left end ensures precise alignment between the through-hole slip ring rotor and the light-shaft transmission shaft, with precision bearings ensuring low-friction rotation;
2. Wiring management system: Dual-row through-hole arrays are set along the side in the front–back direction for safely wiring the through-hole slip ring stator windings. Threaded hole sets on the vertical sides ensure precise positioning and assembly with the hollow connection frame;
3. Integrated support frame: The right-end extension structure has four mounting holes for multi-directional support. The square opening integrates the optical encoder cable channel;

4. Modular protection system: The entire component is made from 6061-T6 aluminum alloy, with O-ring grooves in critical areas.

2.5. Selection of Instrument Modules

2.5.1. Selection of Through-Hole Slip Rings

The CSR in the hollow assembly plays a role in signal transmission. Based on the technical specifications, this study selects a representative and widely applicable through-hole slip ring, model H0835-0605TC from SenriPu. This model has six channels and supports a current of 2 A, a torque of 0.1 N·m, and a contact resistance variation of no more than 10 mΩ. The actual product is shown in Figure 15.



Figure 15. Actual image of H0835-0605TC through-hole slip ring.

2.5.2. Selection of Optical Encoders

The encoder in the hollow assembly is used for monitoring parameters such as angular position and movement. Based on the technical specifications, this study selects a representative and widely applicable optical encoder, model RDE38BS6-12-2-SBG, an absolute optical encoder. This model has a range of 360°, a resolution of 320″, an accuracy of 640″, an SSI communication protocol, and a torque of 0.03 N·m. The actual product is shown in Figure 16.



Figure 16. Actual image of RDE38BS6-12-2-SBG absolute optical encoder.

3. Finite Element Simulation Analysis

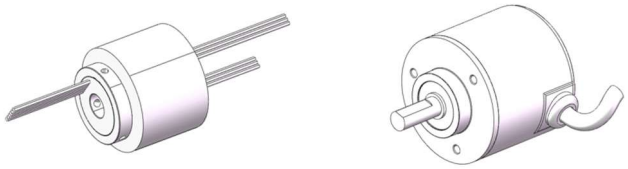
3.1. Establishment of the Assembly Simulation Model

3.1.1. Establishment of the 3D Model

In this study, the fully parametric 3D modeling of the hollow assembly is completed on the SOLIDWORKS platform. Precise geometric interfaces are created to achieve multi-component collaborative assembly. During the modeling process, it was found that the complete detailed model contains over 200,000 geometric features. Directly importing this into simulation software would result in excessive resource consumption and convergence errors. Therefore, a hierarchical simplification strategy is proposed: for key components such as through-hole slip rings and optical encoders, a selective feature retention method

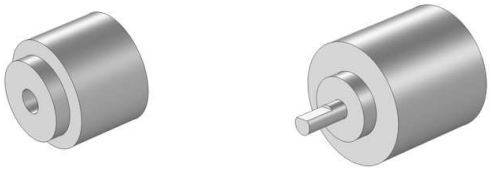
is employed to perform geometric optimization while ensuring functional accuracy. This strategy significantly improves the feasibility of the simulation.

Figures 17 and 18 show the 3D models of the through-hole slip ring and optical encoder before and after simplification, respectively. To achieve more accurate simulation, the rotor and stator of the through-hole slip ring are simplified using two solid bodies. Redundant lines and holes are removed by forming composite surfaces, ignoring edges, and deleting holes to facilitate subsequent meshing. The simplified structure of the through-hole slip ring remains essentially unchanged. The optical encoder, used to measure rotational angular displacement, undergoes similar simplification.



(**a**) (**b**)

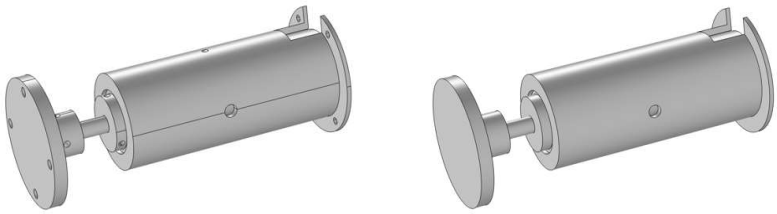
Figure 17. Three-dimensional model before simplification. (**a**) Through-hole slip ring; (**b**) optical encoder.



(**a**) (**b**)

Figure 18. Three-dimensional model after simplification. (**a**) Through-hole slip ring; (**b**) optical encoder.

Figure 19 shows the three-dimensional model diagrams of the hollow assembly before and after simplification. After simplifying the through-hole slip ring and optical encoder, other components also need to be appropriately simplified. The same methods, such as hole deletion, composite surface formation, and edge ignoring, are applied to equivalently simplify the remaining components. Small chamfer features are merged, ultimately forming a lightweight model with multiple consistent boundary pairs. After the simplification, full degrees of freedom are applied as boundary conditions on the two ends of the model, and the gravitational acceleration direction is defined.



(**a**) (**b**)

Figure 19. Hollow assembly model before and after simplification. (**a**) Before simplification; (**b**) after simplification.

3.1.2. Determination of Material Properties

The stability of the assembly structure is closely related to the material properties. During the simulation, empty materials are added at the material nodes, and the material properties of the components are set based on actual 45 steel. Its density is 7810 kg/m^3, its Young's modulus is 200.1 GPa, and its Poisson's ratio is 0.269. For the through-hole slip ring, closed-hole slip ring, and optical encoder, structural steel is used as an equivalent

replacement. After simplifying the model, their corresponding volumes are measured as 2.5266×10^{-5} m^3, 7.0381×10^{-5} m^3, and 4.3341×10^{-5} m^3. Using the mass and volume formula, their corresponding densities are set to 1583 kg/m^3, 2970 kg/m^3, and 2999 kg/m^3. Table 1 shows the mechanical property parameters of the assembly materials [30].

Table 1. Mechanical property parameters of assembly materials.

Materials	Density	Young's Modulus	Poisson's Ratio	Yield Limit	Strength Limit
45 steel	ρ/kg/m^3 7810	E/GPa 200.1	μ 0.269	σ_s/MPa 355	σ_b/MPa 696.6

3.1.3. Mesh Generation Processing

The meshing of the assembly is a critical step in simulation analysis, with mesh quality directly influencing the accuracy of the simulation results. The mesh element sizes are classified into multiple levels: extremely fine, ultra-fine, finer, fine, normal, coarse, coarser, ultra-coarse, and extremely coarse. Finer meshes yield more accurate simulation results but require significantly longer computation times; conversely, coarser meshes reduce computational time at the expense of simulation accuracy. Therefore, selecting an appropriate mesh refinement level ensures a balance between computational efficiency and result accuracy. Considering both simulation accuracy and computational resources, the hollow assembly structure is meshed using finer free tetrahedral elements.

As shown in Figure 20, the mesh distribution is relatively uniform, with green-dominated quality indicating element quality values close to 1 and almost no red elements. The element quality histogram shows black areas concentrated on the right side, confirming that the mesh quality meets the required simulation accuracy. The complete mesh of the hollow assembly comprises 75,409 vertices, 362,251 tetrahedral elements, 58,524 triangles, 3212 edge elements, and 166 vertex elements.

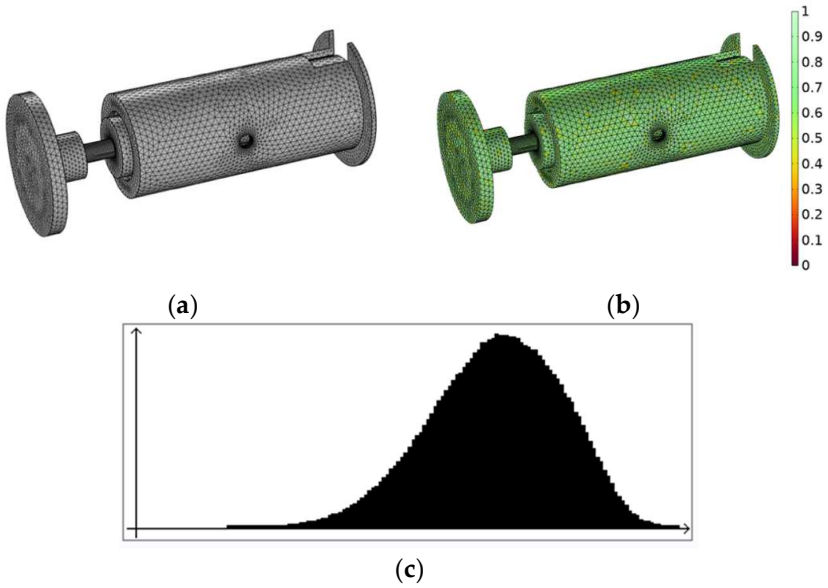
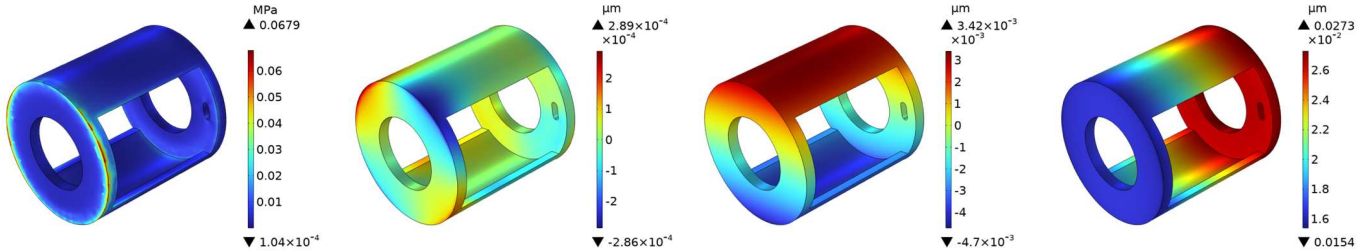


Figure 20. Mesh quality distribution of the hollow assembly. (**a**) Mesh distribution; (**b**) mesh quality map; (**c**) element quality histogram.

3.2. Static Simulation Analysis of the Hollow Assembly

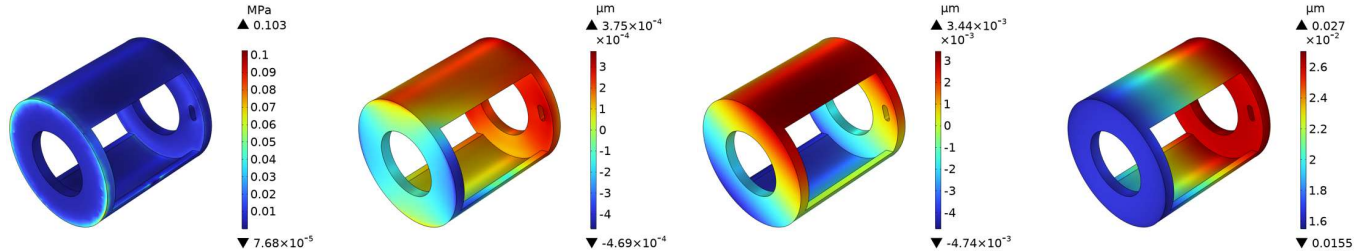
3.2.1. Effect of Assembly Angles of the Hollow Connector Frame on Assembly Accuracy

The machining of the hollow connector frame inevitably introduces errors, which in turn affect the coaxiality during assembly. For the specific assembly structure, the custom-designed sleeve-type coupling (rigid coupling) requires enhanced structural stability, and the adjustment of assembly angles can compensate for machining deviations [31]. Since the hollow assembly is horizontally positioned during installation, the hollow connector frame is subjected to varying gravitational components at different assembly angles. To explore the optimal assembly configuration, a rational simulation analysis of this structure is necessary. Based on the structural characteristics of the hollow connector frame, its assembly angles were set to 0°, 45°, and 90° for comparative analysis (Figure 21 corresponds to 0°, while Figures 22 and 23 maintain consistent positioning for comparison). The von Mises stress and displacement distributions were observed accordingly.



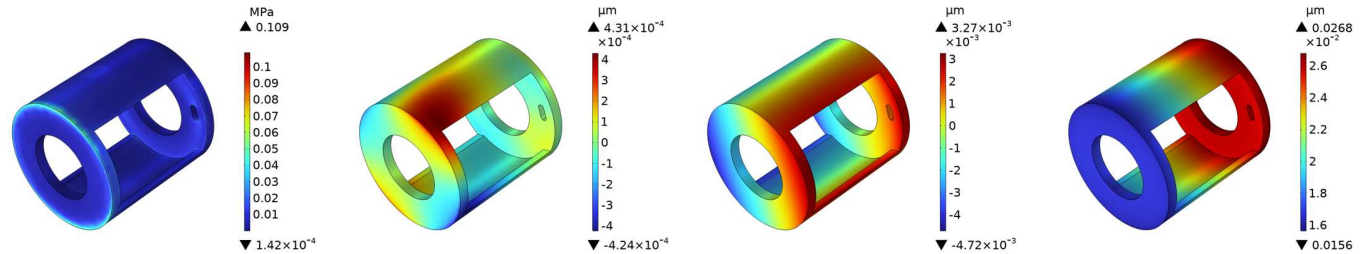
(**a**) (**b**) (**c**) (**d**)

Figure 21. Von Mises stress and XYZ displacement contours at a 0° assembly angle. (**a**) Von Mises stress cloud map; (**b**) X-direction displacement cloud map; (**c**) Y-direction displacement cloud map; (**d**) Z-direction displacement cloud map.



(**a**) (**b**) (**c**) (**d**)

Figure 22. Von Mises stress and XYZ displacement contours at a 45° assembly angle. (**a**) Von Mises stress cloud map; (**b**) X-direction displacement cloud map; (**c**) Y-direction displacement cloud map; (**d**) Z-direction displacement cloud map.



(**a**) (**b**) (**c**) (**d**)

Figure 23. Von Mises stress and XYZ displacement contours at a 90° assembly angle. (**a**) Von Mises stress cloud map; (**b**) X-direction displacement cloud map; (**c**) Y-direction displacement cloud map; (**d**) Z-direction displacement cloud map.

To facilitate comparison, the maximum von Mises stress and displacements in the XYZ directions at different assembly angles were extracted and summarized in Table 2.

Table 2. Maximum von Mises stress and displacement under different assembly angles of the hollow connecting frame.

Angle /°	X-Direction /μm	Y-Direction /μm	Z-Direction /μm	Total Displacement /μm	Von Mises Stress /MPa
0	0.0003	0.0034	0.0273	0.0276	0.0679
45	0.0004	0.0034	0.0270	0.0273	0.1030
90	0.0004	0.0033	0.0268	0.0271	0.1090

Table 2 presents the maximum von Mises stress and displacement values of the hollow connector frame under different assembly angles. According to the data, the stress is minimal at the 0° assembly angle, while the directional and total displacements show relatively minor variations. Therefore, adopting a 0° assembly angle in practice can ensure optimal assembly accuracy. These simulation results provide theoretical guidance for subsequent structural analyses and performance testing.

3.2.2. Influence of Gravity on the Structural Stability of the Assembly

Due to the structural complexity of the hollow assembly, conventional mechanical analysis is insufficient for accurately determining the magnitudes of von Mises stress and displacement. Therefore, it is necessary to identify the vulnerable regions of the structure and obtain relevant data on von Mises stress and displacement. The hollow assembly remains in a horizontal position after assembly, and its stability during operation is affected by gravitational loading. It is thus necessary to analyze the overall deformation of the assembly to assess the structural loading conditions and their impact on stability.

As shown in Figure 24, under self-weight conditions, the assembly exhibits a typical gradient stress distribution. The maximum von Mises stress, 0.913 MPa, occurs at the contact edge of the optical shaft, corresponding to a safety factor of 388.8. The local enlarged view of its von Mises stress cloud diagram is shown in Figure 25. All stress maxima in the components are significantly lower than the yield strength of 45 steel (355 MPa). Secondary stress concentration zones are observed at the inner edge of the sleeve coupling (0.245 MPa), the wire outlet of the through-hole slip ring (0.588 MPa), and the shaft of the photoelectric encoder (0.328 MPa) but are all within the elastic deformation range. This stress distribution pattern confirms the effectiveness of the stiffness matching design between the rigid coupling and the hollow connector frame.

Displacement field analysis (Figure 26) shows that the assembly undergoes coordinated deformation under gravity. The maximum displacement of 0.0316 μm occurs at the coupling region between the slip ring and the drive shaft, meeting micron-level assembly precision standards. Analysis of the key components reveals a maximum displacement gradient between the guide sleeve (0.0316 μm) and the small-hole adapter plate (0.00615 μm), with a displacement ratio of 5.14. This confirms the deformation coordination capability of the modular design. All component displacement contours exhibit axial symmetry, further confirming the balanced stiffness distribution of the overall structure.

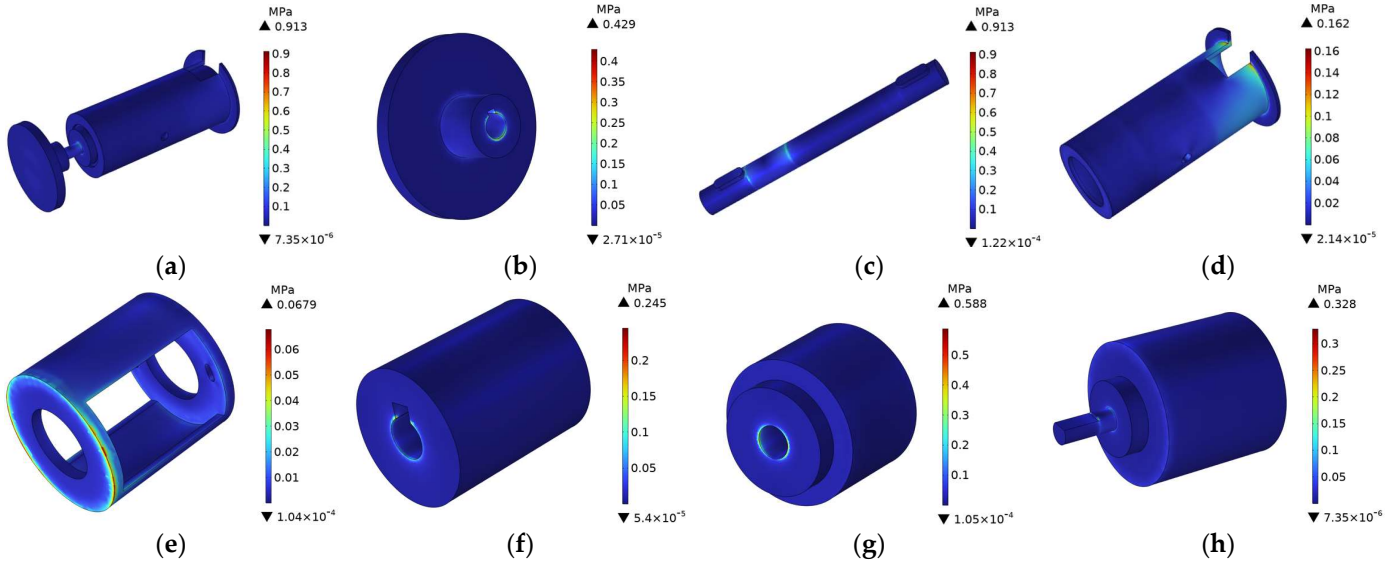


Figure 24. Von Mises stress distribution of the entire hollow assembly and key components. (**a**) Overall von Mises stress nephogram; (**b**) perforated adapter plate; (**c**) optical shaft drive shaft; (**d**) bush-type fixed cover; (**e**) hollow connecting frame; (**f**) sleeve coupling; (**g**) through-hole slip ring; (**h**) photoelectric encoder.

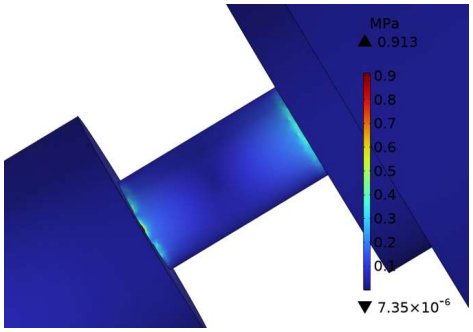


Figure 25. Local magnification of von Mises stress distribution in the hollow assembly.

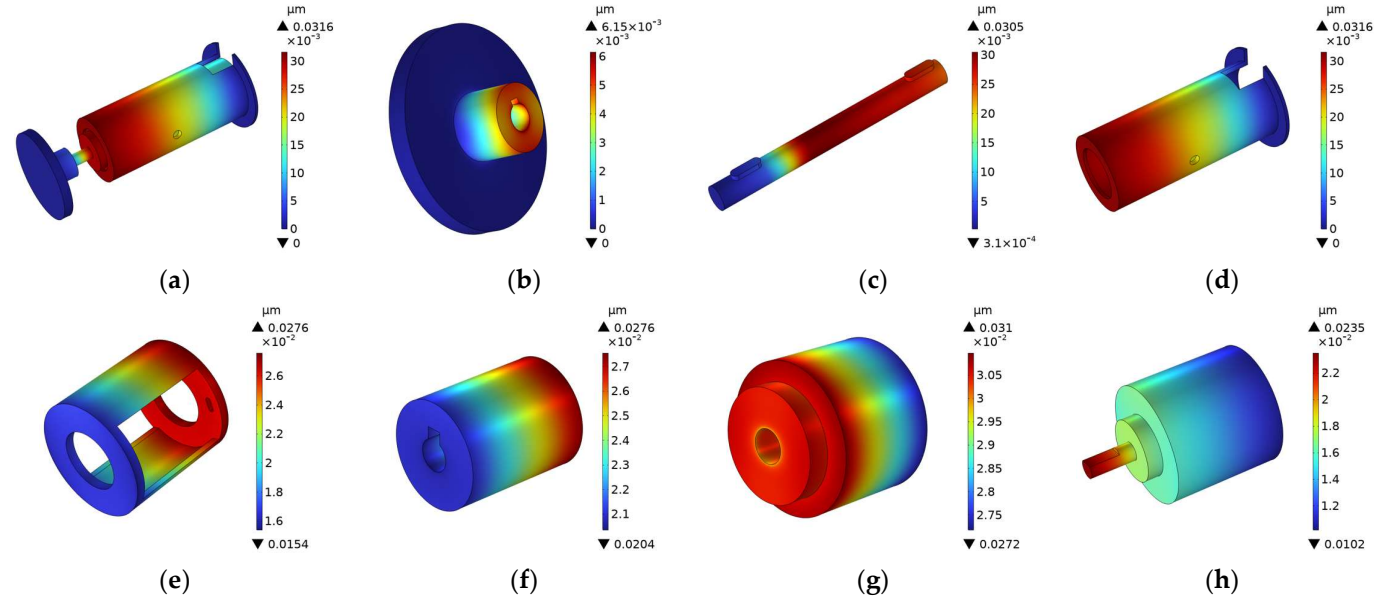


Figure 26. Displacement distribution of the entire hollow assembly and key components. (**a**) Global displacement cloud image; (**b**) perforated adapter plate; (**c**) optical-shaft drive shaft; (**d**) bush-type fixed cover; (**e**) hollow connecting frame; (**f**) sleeve coupling; (**g**) through-hole slip ring; (**h**) photoelectric encoder.

3.3. Modal Analysis of the Dynamic Characteristics of the Hollow Assembly

The clamping module of the hollow assembly adopts two types of fixed structures: a hollow connecting frame and a flange-type connecting frame. During operation with rotational equipment, inevitable vibrations occur in the system. To investigate the resonance characteristics and comparative structural stability, a modal analysis was performed to determine the natural frequencies at which resonance may occur for each configuration, as shown in Figures 27 and 28. Given the miniaturized structure of the hollow assembly, and based on findings in [32], the resonance phenomenon in small motors generally occurs within the low-to-medium frequency range. Therefore, extracting the first six modal modes is sufficient to evaluate the dynamic characteristics and ensure the structural stability of the assembly.

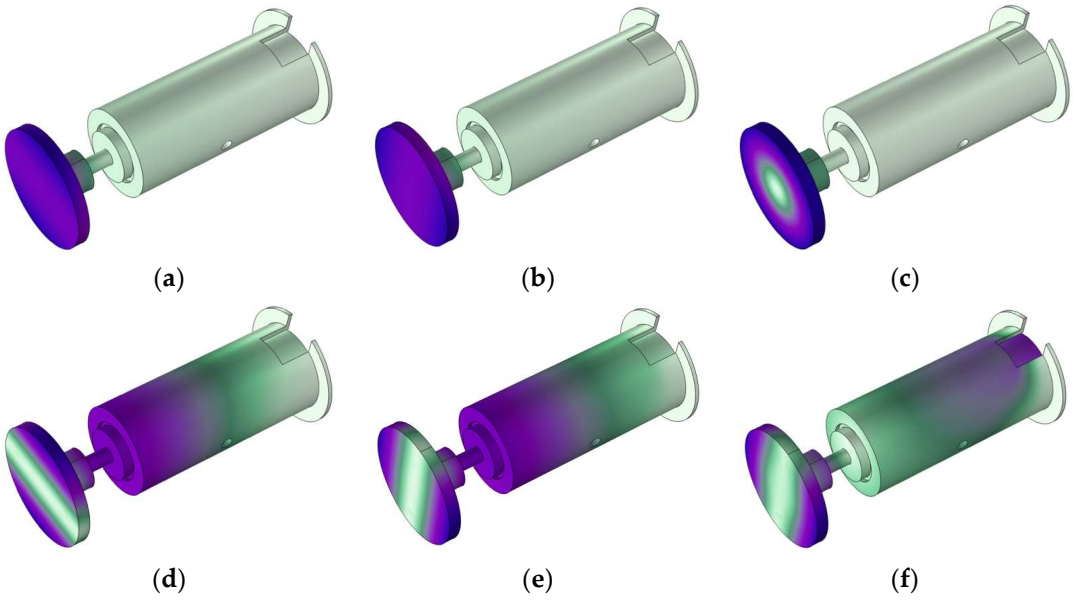


Figure 27. Six-order modal diagram of the whole fixed structure of the hollow connecting frame. (**a**) First-order modal diagram; (**b**) second-order modal diagram; (**c**) third-order modal diagram; (**d**) fourth-order modal diagram; (**e**) fifth-order modal diagram; (**f**) sixth-order modal diagram.

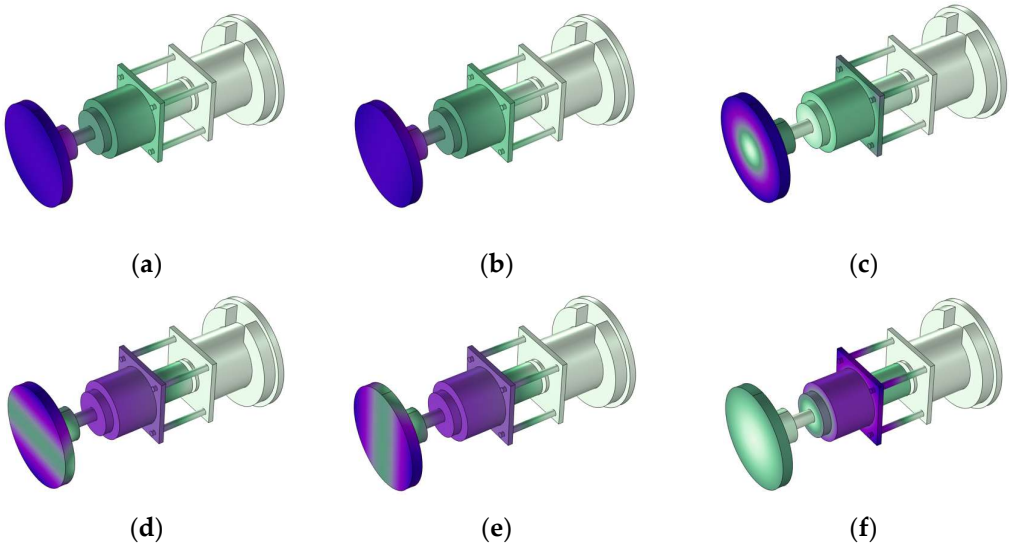


Figure 28. Six-order modal diagram of the whole fixed structure of the flanged connecting frame. (**a**) First-order modal diagram; (**b**) second-order modal diagram; (**c**) third-order modal diagram; (**d**) fourth-order modal diagram; (**e**) fifth-order modal diagram; (**f**) sixth-order modal diagram.

Based on the modal simulation results, the natural frequencies and vibration mode characteristics of the hollow and flange-type connecting frame structures were extracted for each mode and summarized in Table 3.

Table 3. Natural frequencies and dangerous areas of the first six modes of the fixed structure of the two connection frames.

Order	1	2	3	4	5	6
Natural frequency (Hollow-type)	585.24	590.45	846.49	1903.30	2006.20	4431.20
Danger area (Hollow-type)	Small-hole-type transfer plate on both sides	Small-hole-type transfer plate left and right sides	Eyelet adapter plate outer edge area	Small-hole-type adapter plate up and down and through-hole-type slip ring area	Small-hole-type adapter plate left and right and through-hole-type slip ring area	The left and right side of the pinhole transfer plate and the photoelectric encoder area
Natural frequency (Flange-type)	409.98	411.69	625.92	979.18	981.84	1682.40
Danger area (Flange-type)	Access area of the small-hole adapter board	Access area of the small-hole adapter board	Eyelet adapter plate outer edge area	Small-hole-type adapter plate and through-hole-type slip ring flange area	Small-hole-type adapter plate left and right and through-hole-type slip ring flange area	Pass-type slip ring flange and fixed-rod part area

Table 3 lists the first six natural frequencies and corresponding critical regions for both structural configurations. The results indicate that the first six natural frequencies of the hollow and flange-type connecting frame structures range from 585.24 Hz to 4431.20 Hz and from 409.98 Hz to 1682.40 Hz, respectively. Although both structures exhibit natural frequencies above the design threshold of 400 Hz, the hollow connecting frame demonstrates a higher excitation frequency range and superior vibration stability, thereby ensuring greater operational reliability of the assembly. Thus, the findings from this simulation provide valuable guidance for future performance evaluations.

4. Performance Testing of the Hollow-Type Integrated Assembly

4.1. Assembly Platform Construction

To meet the technical requirements of the integrated assembly, the design of the test platform must fulfill the following criteria:

1. Precision: The test platform must ensure the precision necessary for evaluating the assembly's operational accuracy. It is essential to select an appropriate reference datum and minimize assembly errors that might impact measurement accuracy;
2. Stability: As the foundation for the system's operational reliability and the accuracy of test data, the platform must incorporate a structurally stable rotational mechanism;
3. Versatility: Given the structural diversity of potential assemblies, the platform should accommodate various assembly types, enabling flexible installation and clamping configurations.

Considering the real-world working conditions of the assembly, a comprehensive experimental setup was developed, as shown in Figure 29. This platform exhibits a combi-

nation of precision, stability, and adaptability that is suitable for the performance testing of the hollow-type integrated assembly.

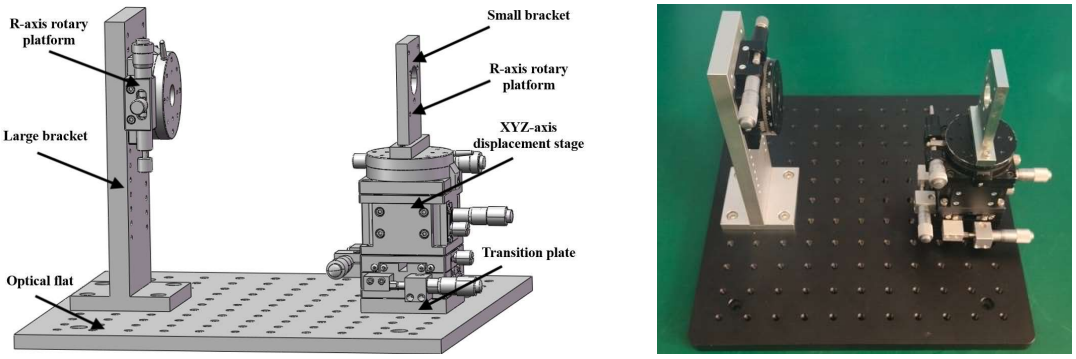


Figure 29. Test platform design. (**a**) Three-dimensional model view; (**b**) physical setup.

The platform comprises three major subsystems: the support module, displacement module, and digital display module. The support module includes a large and small bracket. The large bracket connects the optical flat with the R-axis rotary platform, while the small bracket links the rotary platform with the assembly. The displacement module integrates the R-axis rotary platform, XYZ-axis displacement stage, and a transition plate, all mounted on the optical flat. The digital display module consists of a DC micro-ohmmeter and a digital readout system. During testing, the R-axis rotary platform drives the assembly's rotation, and performance metrics are acquired by monitoring the digital readouts. The following sections elaborate on the calibration of the rotary platform and the structural design and selection of key components.

The experimental design is based on the assumption that the proposed hollow-type integrated assembly design will outperform conventional designs in contact resistance, angular repeatability, and accuracy. This assumption is supported by finite element analysis results and the principles of mechanical transmission and structural optimization. The R-axis rotary table was chosen for testing due to its high-precision angular measurement and control capabilities, which match the study's objective of evaluating the assembly's performance under precise rotational conditions.

4.1.1. Calibration of the Rotating Platform

During initial angle measurements using the R-axis platform and the optical encoder, two critical calibration deficiencies were identified: 1. absence of a defined mechanical zero reference for the platform and 2. a non-zero initial reading on the encoder display. To establish an accurate measurement reference, a coaxial dual-axis calibration method was employed. The axial alignment between the R-axis rotary platform and the encoder serves as the reference baseline, as illustrated in Figure 30.

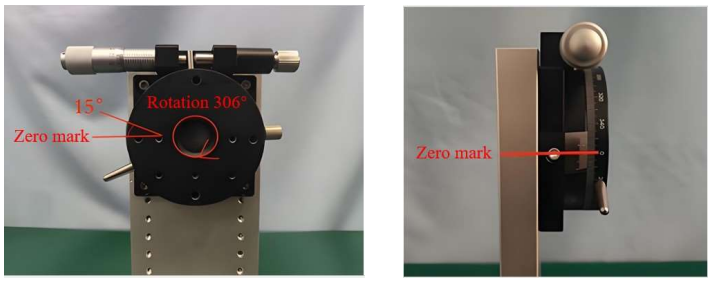
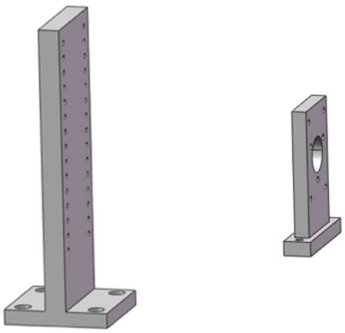


Figure 30. R-axis rotary platform calibration reference. (**a**) Front view; (**b**) side view.

The calibration follows a three-level precision control strategy: First, the platform's zero mark is aligned with a horizontal reference plane and the fixture is oriented so that the normal vector is perpendicular to gravity. Next, fine adjustments are made using a mechanical micro-adjustment mechanism ($\pm 5'$ precision) and optical alignment to ensure sub-pixel accuracy between the fixed and rotating parts. Simultaneously, the encoder display is reset via a hardware command using the RS485 interface. After initialization, circular tests are conducted according to ISO 9283-1998 [33], with 15° step increments across a full rotation. After each cycle, the system is recalibrated using a self-alignment protocol. Laser interferometry verification confirms an angular positioning accuracy of $72''$, satisfying the technical requirements of the assembly.

4.1.2. Design of the Support Module

As the assembly is horizontally mounted, support structures are essential for proper positioning. Based on the structural and dimensional characteristics of the assembly, the large and small brackets were designed accordingly, as shown in Figure 31.

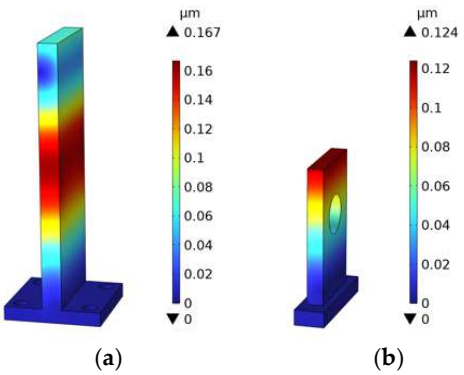


(**a**) (**b**)

Figure 31. Three-dimensional models of brackets. (**a**) Large bracket; (**b**) small bracket.

The large bracket has an inverted T-shape structure featuring countersunk holes at the base and threaded holes along the sidewalls. It is fixed to the optical flat and R-axis platform using screws, with the side threads allowing height adjustments. The small bracket, also an inverted T-shaped, has through-holes at the base and threaded/center holes along the side. It connects the R-axis platform and the protection module, with the central hole reserved for encoder cabling.

As shown in Figure 32, the maximum deformation of the large bracket occurs at the central region, reaching 0.167 μm, while the small bracket deforms most at the top, with a maximum displacement of 0.124 μm. These minimal deformations ensure reliable contact interfaces and negligible impact on assembly precision, thereby validating the structural stability and reliability of the support system.

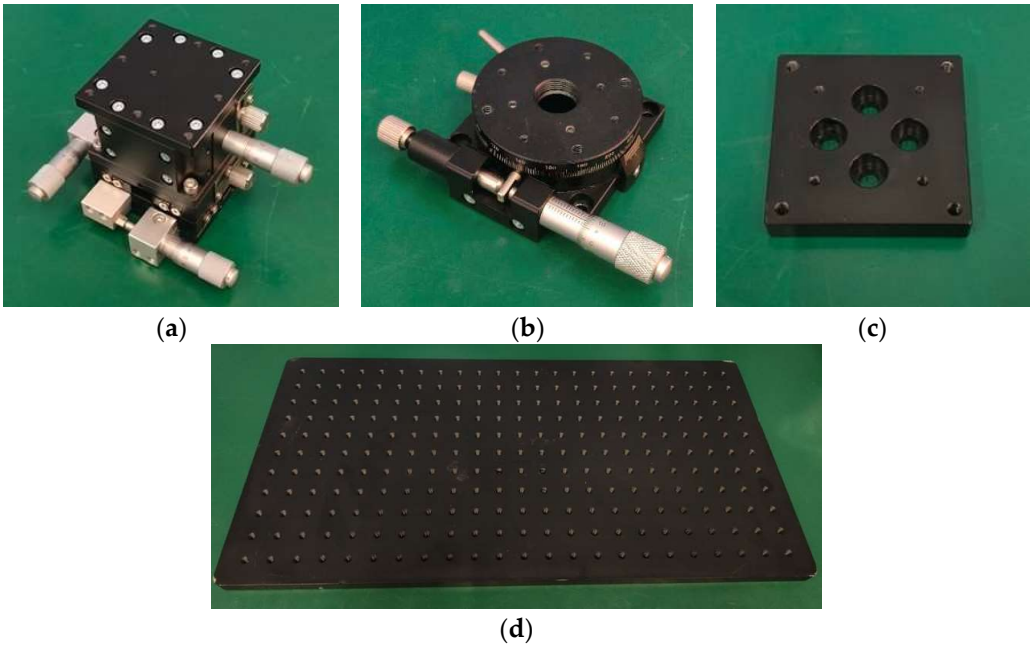


(**a**) (**b**)

Figure 32. Displacement simulation results of brackets. (**a**) Large bracket; (**b**) small bracket.

4.1.3. Selection of the Displacement Module

To minimize installation errors during performance testing, a displacement mechanism was required for positional adjustments. The selected components include LD60-LM-2 XYZ-axis displacement stage, RSP60-L R-axis rotary platform, 60 mm × 60 mm × 10 mm transition plate, and 600 mm × 300 mm × 13 mm optical flat. Physical views of these components are presented in Figure 33, with the detailed performance parameters summarized in Tables 4 and 5.



(**a**) (**b**) (**c**) (**d**)

Figure 33. Physical images of the displacement module. (**a**) XYZ-axis displacement platform; (**b**) R-axis rotation platform; (**c**) displacement platform switching plate; (**d**) optical plate.

Table 4. Performance parameters of LD60-LM-2 XYZ-axis displacement platform.

XYZ-Axis Displacement Platform Model	LD60-LM-2
XY-stroke	±6.5 mm
Z-stroke	10 mm
Minimum scale	0.01 mm
Precision	0.03 mm
Parallelism	0.03 mm

Table 5. Performance parameters of RSP60-L R-axis rotating platform.

R-Axis Rotary Platform Model	RSP60-L
Mesa size	ϕ60
Journey	360° coarse adjustment, ±5° fine adjustment
Angular accuracy	72″
Minimum scale	5 mm
Concentricity	0.02 mm
Parallelism	0.02 mm

4.1.4. Selection of the Digital Display Module

The performance evaluation of the CSR primarily relies on key indicators such as contact resistance fluctuation, signal transmission loss, and wear resistance. To verify whether the assembly meets the technical specifications, this study focuses on testing the

slip ring's contact resistance fluctuations. Currently, the common methods for measuring contact resistance include the volt–ampere method, the four-wire method, and the micro-ohmmeter method. Considering both measurement accuracy and practical requirements, the four-wire method is adopted in this study to effectively minimize the influence of lead resistance on the test results. The EX680B DC low-resistance meter is selected as the testing instrument in this study. This device operates without an external power supply and can directly measure contact resistance, making it suitable for high-precision measurements under conditions without external current input. During testing, the wires at both ends of the CSR are connected to the resistance meter to obtain the contact resistance and its fluctuation range, thereby verifying compliance with the technical specifications. The experimental setup is shown in Figure 34, and relevant performance parameters are detailed in Table 6.



Figure 34. EX680B-type DC low-resistance meter diagram.

Table 6. Performance parameters of EX680B DC low-resistance meter.

DC Low-Resistance Meter Model	EX680B
Resistance range	0.001 mΩ∼30 KΩ
Resolution	1 μΩ
Precision	±0.1%FS
Detection method	Four-wire test
Test current	≥1A

The performance evaluation of the photoelectric encoder mainly focuses on key indicators such as angular accuracy, resolution, and angular repeatability. To verify the technical conformity of the assembly, this study conducts performance testing by measuring the encoder's rotational angular displacement. Currently, the display methods for angular displacement testing include lower-computer and upper-computer display schemes. Based on the practical testing conditions and requirements, this study adopts the lower-computer display method, connecting the photoelectric encoder to the digital display module via the SSI communication protocol to directly obtain rotational angular displacement data. The WF770X digital display meter (SSI serial data controller) is selected as the testing instrument, with its appearance shown in Figure 35.



Figure 35. WF770X digital display table.

4.2. Assembly Sequence of the Hollow-Type Integrated Structure

Given the numerous components involved in the hollow-type assembly, a well-defined assembly sequence is crucial. The physical components are shown in Figure 36. The assembly process begins with component preparation and concludes upon passing performance testing. The through-hole slip ring and photoelectric encoder are assembled separately, followed by final integration. The detailed assembly steps are as follows:

1. Mount the optical-shaft-type drive shaft inside the rotor of the through-hole slip ring, ensuring that the side with the keyway is near the slip ring stator lead;
2. Attach the sleeve-type coupling to the drive shaft on the side close to the keyway;
3. Install the side of the hollow connector frame with a straight slot at the stator lead area of the through-hole slip ring and guide the wires through the slot;
4. Mount the photoelectric encoder onto the hollow connector frame, inserting its rotating shaft into the sleeve coupling;
5. Insert the guide sleeve-type protective cover from the lead end of the slip ring rotor and route the wires through the wiring hole;
6. Mount the small-hole-type adapter plate onto the drive shaft to complete the assembly.

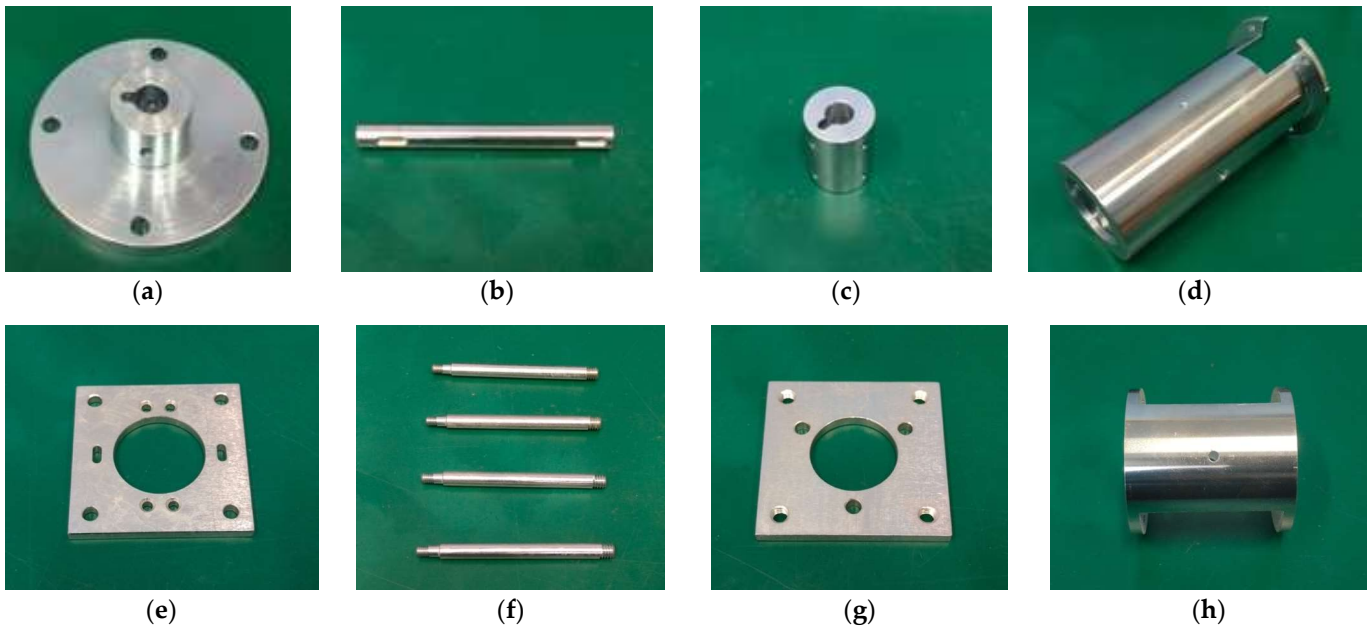


Figure 36. Physical components of the hollow-type integrated assembly. (**a**) Small-hole-type adapter plate; (**b**) optical-shaft-type drive shaft; (**c**) sleeve-type coupling; (**d**) guide-sleeve protective cover; (**e**) through-hole slip ring flange; (**f**) fixed connecting rod; (**g**) photoelectric encoder flange; (**h**) hollow connector frame.

After assembly, the hollow-type structure is mounted on the test platform, as shown in Figure 37. Subsequent tests are conducted to evaluate contact resistance and rotational angle performance. The rotational angle tests include comparisons of different transmission and fixation methods, as well as assessments of angular repeatability and accuracy. All tests are conducted under standard environmental conditions.

4.3. Contact Resistance Test of the Hollow-Type Integrated Structure

Signal transmission stability is a key indicator for evaluating the performance of the hollow-type integrated structure. To investigate the effect of shaft radial runout during rotation on electrical conduction, a dedicated contact resistance test was designed. The test requirement stipulates that within the full 0–360° rotation range, the contact resistance

variation must remain within 10 mΩ to satisfy technical performance criteria. An R-axis rotary platform was used to perform full-circle measurements at 15° intervals. The test was conducted on six circuits within the assembly, identified by white, green, blue, red, black, and yellow wires. The contact resistance at each rotation angle was measured for all circuits, and the resulting variation curves are presented in Figure 38.



(**a**) (**b**)

Figure 37. Overall assembly and test platform design of the hollow-type integrated structure. (**a**) Three-dimensional model; (**b**) physical view.

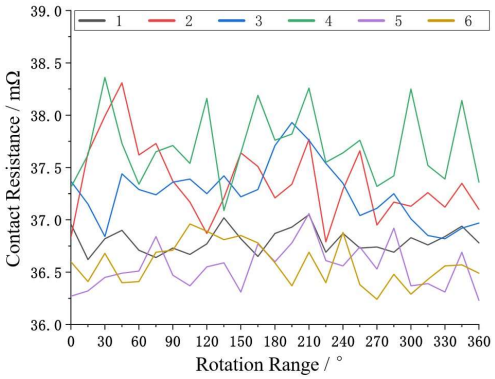


Figure 38. Variation of contact resistance for six circuits at different rotation angles.

Figure 38 illustrates the contact resistance variation of the six circuits at different angles. The test results show that the contact resistance for channels 1 to 6 (corresponding to white, green, blue, red, black, and yellow wires) remains within the range of 36.23–38.76 mΩ. Analysis suggests that the observed fluctuations are primarily caused by the structural characteristics of the assembly. The rotor of the through-hole slip ring is interference-fitted with the optical drive shaft, which inevitably leads to radial runout during rotation. This induces micro-vibrations at the brush–ring contact interface, resulting in resistance fluctuations. Nevertheless, the contact resistance variation for all circuits remains within 10 mΩ, fully meeting the technical specifications.

4.4. Rotational Angle Testing of the Hollow-Type Integrated Assembly

4.4.1. Comparative Test of Different Transfer Modes of Hollow Assembly

To investigate the effect of coupling types on the transmission accuracy of the hollow-type assembly, three representative structures were selected for comparison: the standard wire-wound coupling, the wire-wound clamping coupling, and a self-designed sleeve-type coupling. Figure 39 shows the prototypes of the three couplings: the standard wire-wound coupling, the wire-wound clamping coupling, and the innovatively designed sleeve-type coupling.



(**a**) (**b**) (**c**)

Figure 39. Physical prototypes of couplings. (**a**) Wire-wound coupling; (**b**) wire-wound clamping coupling; (**c**) sleeve-type coupling.

The R-axis rotary platform was rotated every 15° for a full revolution to conduct comparative tests of the three couplings at various angular displacements. The results are presented in Tables 7–9.

Table 7. Angle test of winding coupling assembled by hollow assembly.

Rotational Angular Displacement /″	Test Angular Displacement /″	Absolute Error /″
54,000	53,485.2	−514.8
108,000	107,920.8	−79.2
162,000	162,669.6	+669.6
216,000	215,841.6	−158.4
270,000	269,326.8	−673.2
324,000	324,075.6	+75.6
378,000	378,511.2	+511.2
432,000	432,630.0	+630.0
486,000	485,485.2	−514.8
540,000	539,604.0	−396.0
594,000	594,669.6	+669.6
648,000	647,841.6	−158.4
702,000	702,273.6	+273.6
756,000	756,392.4	+392.4
810,000	809,564.4	−435.6
864,000	863,683.2	−316.8
918,000	918,115.2	+115.2
972,000	972,234.0	+234.0
1,026,000	1,026,352.8	+352.8
1,080,000	1,079,524.8	−475.2
1,134,000	1,133,960.4	−39.6
1,188,000	1,188,075.6	+75.6
1,242,000	1,242,511.2	+511.2
1,296,000	1,296,630.0	+630.0

Comparative analysis of the data in Tables 7–9 shows that the assembly using the wire-wound clamping coupling exhibits the largest absolute angular displacement error, whereas the self-designed sleeve-type coupling significantly reduces this error and fully meets the technical specifications. The observed differences are primarily attributed to two factors: (1) the wire-wound clamping coupling tends to wobble under dynamic conditions and improper torque during assembly may lead to installation eccentricity and (2) the sleeve-type coupling features optimized structural design, offering superior mechanical stability and assembly precision.

Table 8. Angle test of hollow assembly wound-clamp coupling.

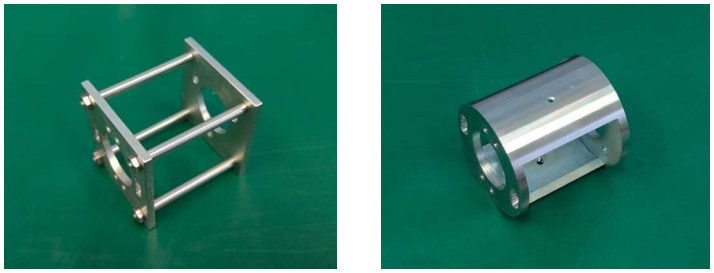
Rotational Angular Displacement /″	Test Angular Displacement /″	Absolute Error /″
54,000	53,485.2	−594.0
108,000	107,287.2	−712.8
162,000	161,722.8	−277.2
216,000	216,154.8	+154.8
270,000	270,590.4	+590.4
324,000	324,709.2	+709.2
378,000	377,247.6	−752.4
432,000	431683.2	−316.8
486,000	486,432.0	+432.0
540,000	540,234.0	+234.0
594,000	593,722.8	−277.2
648,000	647,841.6	−158.4
702,000	701,960.4	−39.6
756,000	756,392.4	+392.4
810,000	809,247.6	+752.4
864,000	863,366.4	+633.6
918,000	917,802.0	−198.0
972,000	972,234.0	+234.0
1,026,000	1,026,352.8	+352.8
1,080,000	1,080,788.4	+788.4
1,134,000	1,133,326.8	−673.2
1,188,000	1,188,392.4	+392.4
1,242,000	1,241,564.4	−435.6
1,296,000	1,295,683.2	−316.8

Table 9. Angle test of hollow assembly with matching cylinder coupling.

Rotational Angular Displacement /″	Test Angular Displacement /″	Absolute Error /″
54,000	53,802.0	−198.0
108,000	107,604.0	−396.0
162,000	161,722.8	−277.2
216,000	215,841.6	−158.4
270,000	269,960.4	−39.6
324,000	324,075.6	+75.6
378,000	378,511.2	+511.2
432,000	431,366.4	−633.6
486,000	485,485.2	−514.8
540,000	540,550.8	+550.8
594,000	593,722.8	−277.2
648,000	648154.8	+154.8
702,000	702,273.6	+273.6
756,000	756,392.4	+392.4
810,000	809,881.2	−118.8
864,000	864,630.0	+630.0
918,000	918,115.2	+115.2
972,000	971,920.8	−79.2
1,026,000	1,025,722.8	−277.2
1,080,000	1,079,841.6	−158.4
1,134,000	1,134,273.6	+273.6
1,188,000	1,188,392.4	+392.4
1,242,000	1,241,564.4	−435.6
1,296,000	1,296,313.2	+313.2

4.4.2. Comparative Study of Fixation Methods on the Transmission Accuracy of the Hollow-Type Assembly

Test results indicate that the self-designed sleeve-type coupling exhibits the best transmission performance. Given the high sensitivity of the photoelectric encoder to vibration and shock, it is necessary to incorporate a fixation structure at the coupling interface to ensure stable operation. Two fixation schemes were designed for the clamping module, a flange-type connector and a hollow connector, as illustrated in Figure 40. Modal simulation under motor-driven conditions, along with comparative experiments, was used to evaluate how different fixation structures affect the transmission accuracy of the sleeve-type coupling. The hollow connector, when combined with the optimal assembly approach, demonstrated superior dynamic stability.



(**a**) (**b**)

Figure 40. Physical prototypes of connectors. (**a**) Flange-type connector; (**b**) hollow connector.

The R-axis rotary platform was rotated in 15° increments for a full revolution to compare the two connector types under different angular displacements. The test results are presented in Tables 10 and 11.

Table 10. Angle test of hollow assembly flange connecting frame.

Rotational Angular Displacement /″	Test Angular Displacement /″	Absolute Error /″
54,000	53,802.0	−198.0
108,000	107,604.0	−396.0
162,000	162,352.8	+352.8
216,000	216,154.8	+154.8
270,000	269,643.6	−356.4
324,000	324,075.6	+75.6
378,000	377,881.2	−118.8
432,000	431,366.4	−633.6
486,000	485,802.0	−198.0
540,000	539,920.8	−79.2
594,000	594,352.8	+352.8
648,000	647,841.6	−158.4
702,000	701,960.4	−39.6
756,000	755,762.4	−237.6
810,000	810,511.2	+511.2
864,000	863,683.2	−316.8
918,000	918,432.0	+432.0
972,000	971,920.8	−79.2
1,026,000	1,025,406.0	−594.0
1,080,000	1,080,154.8	+154.8
1,134,000	1,134,273.6	+273.6
1,188,000	1,188,075.6	+75.6
1,242,000	1,241,881.2	−118.8
1,296,000	1,295,683.2	−316.8

Table 11. Angle test of hollow connecting frame assembled by hollow assembly.

Rotational Angular Displacement /″	Test Angular Displacement /″	Absolute Error /″
54,000	54,115.2	+115.2
108,000	107,920.8	−79.2
162,000	162,026.0	+36.0
216,000	216,471.6	+471.6
270,000	270,273.6	+273.6
324,000	324,392.4	+392.4
378,000	377,881.2	−118.8
432,000	432,000.0	0.0
486,000	486,432.0	+432.0
540,000	539,920.8	−79.2
594,000	594,036.0	+36.0
648,000	647,841.6	−158.4
702,000	702,590.4	+590.4
756,000	755,445.6	−554.4
810,000	809,564.4	−435.6
864,000	863,366.4	−633.6
918,000	917,802.0	−198.0
972,000	971,920.8	−79.2
1026,000	1,026,352.8	+352.8
108,0000	1,079,841.6	−158.4
1,134,000	1,134,590.4	+590.4
1,188,000	1,188,075.6	+75.6
1,242,000	1,242,194.4	+194.4
1,296,000	1,296,630.0	+630.0

As shown in Tables 10 and 11, the difference in maximum absolute angular displacement error between the two fixation structures is not significant, and both meet the technical specifications. The analysis indicates that, under normal working conditions, the type of fixation structure has a limited impact on transmission accuracy. However, modal simulation results confirm that under intense vibration conditions, the hollow connector demonstrates superior dynamic stability and improved vibration damping compared to the flange-type connector. Moreover, its optimized assembly angle enhances the overall assembly precision. Overall, the hollow connector design in this study exhibits significant advantages in terms of dynamic performance and assembly adaptability.

4.4.3. Repeatability Testing of the Hollow-Type Assembly's Angular Displacement

Angular repeatability is a key performance metric for evaluating the motion accuracy of the hollow-type assembly. In this study, a series of tests were conducted to verify angular repeatability. The technical requirement specifies that angular displacement error must be $\leq 500''$ over the full 0–360° range. The R-axis rotary platform was used with 15° intervals to complete full-circle measurements. The test data are shown in Table 12.

Under repeatability conditions, the assembly was tested n times independently at each angular displacement. The repeatability, denoted as $s(y_{i1})$, is calculated as the standard deviation across the n measurements.

$$s(y_{i1}) = \sqrt{\frac{\sum_{i1=1}^{n}(y_{i1} - \overline{y}_1)^2}{n-1}}, \tag{4}$$

In the actual test with n = 5, the maximum repeatability error across all angular positions was $s(y_{i1})_{\max} = 499.8''$, remaining within the required threshold of 500″. This confirms the structural integrity and transmission reliability of the assembly.

Table 12. Angular repeatability test of hollow assembly.

Rotational Angular Displacement /″	1	2	3	4	5	Mean Value
0	0	0	0	0	0	0
54,000	53,485.2	54,115.2	53,168.4	54,432.0	53,802.0	53,800.6
1,080,00	108,867.6	108,234.0	107,604.0	108,550.8	107,920.8	108,235.4
162,000	161,722.8	161,406.0	161,089.2	162,352.8	162,036.0	161,721.4
216,000	216,471.6	215,208.0	215,841.6	216,154.8	215,524.8	215,840.2
270,000	270,590.4	269,643.6	270,907.2	270,273.6	269,960.4	270,275.0
324,000	323,128.8	324,392.4	324,075.6	323,762.4	323,445.6	323,761.0
378,000	378,828.0	377,881.2	378,194.4	377,564.4	378,511.2	378,195.8
432,000	432,313.2	432,000.0	431,683.2	431,366.4	431,049.6	431,682.5
486,000	485,168.4	485,485.2	485,802.0	486,115.2	486,432.0	485,800.6
540,000	540,234.0	540,550.8	539,604.0	539,920.8	540,867.6	540,235.4
594,000	594,352.8	593,406.0	593,089.2	593,722.8	594,036.0	593,721.4
648,000	648,471.6	647,841.6	647,524.8	647,208.0	648,154.8	647,840.2
702,000	702,273.6	702,907.2	701,960.4	702,590.4	701,643.6	702,275.0
756,000	755,128.8	756,075.6	755,762.4	756,392.4	755,445.6	755,761.0
810,000	810,194.4	809,881.2	810,828.0	810,511.2	809,564.4	810,195.8
864,000	863,683.2	864,313.2	863,366.4	864,000.0	863,049.6	863,682.5
918,000	917,802.0	917,168.4	918,115.2	918,432.0	917,485.2	917,800.6
972,000	972,867.6	972,234.0	971,920.8	971,604.0	972,550.8	972,235.4
1,026,000	1,025,722.8	1,026,036.0	1,025,406.0	1,026,352.8	1,025,089.2	1,025,721.4
1,080,000	1,079,524.8	1,080,471.6	1,080,154.8	1,079,208.0	1,079,841.6	1,079,840.2
1,134,000	1,134,907.2	1,134,590.4	1,133,960.4	1,133,643.6	1,134,273.6	1,134,275.0
1,188,000	1,187,445.6	1,187,762.4	1,187,128.8	1,188,392.4	1,188,075.6	1,187,761.0
1,242,000	1,241,564.4	1,242,828.0	1,242,194.4	1,241,881.2	1,242,511.2	1,242,195.8
1,296,000	1,296,313.2	1,295,683.2	1,296,000.0	1,295,049.6	1,295,366.4	1,295,682.5

4.4.4. Angular Accuracy Testing of the Hollow-Type Assembly

Angular accuracy is a critical metric in evaluating the performance of the hollow-type assembly, directly impacting the stability and reliability of the through-hole slip ring. In this study, a series of tests were conducted to validate the assembly's angular accuracy, with the technical requirement set at a maximum error of 720″ over the full 0–360° rotation. The R-axis platform was used to perform 360° measurements in 15° steps. Each point was tested three times to ensure data reliability. Results are shown in Table 13.

Table 13 reveals that the maximum absolute angular displacement error measured was 633.6″. According to Table 6, the inherent rotational accuracy of the R-axis platform is 72″, which contributes to cumulative measurement errors. As deformations in other parts of the platform are negligible, the combined maximum angular error of the hollow-type assembly is calculated to be 705.6″, which remains within the required limit of 720″. These results validate that the designed hollow-type assembly meets the angular accuracy requirements and ensures the reliable operation of the through-hole slip ring.

Table 13. Angular accuracy test of hollow assembly.

Rotational Angular Displacement /″	Test Angular Displacement /″	Absolute Error /″
	54,115.2	+115.2
54,000	53,802.0	−198.0
	54,432.0	+432.0
	107,604.0	−396.0
108,000	108,550.8	+550.8
	108,234.0	+234.0
	162,352.8	+352.8
162,000	161,722.8	−277.2
	162,036.0	+36.0
	216,154.8	+154.8
216,000	216,471.6	+471.6
	215,524.8	−475.2
	270,273.6	+273.6
270,000	269,643.6	−356.4
	269,960.4	−39.6
	324,392.4	+392.4
324,000	323,445.6	−554.4
	324,075.6	+75.6
	377,881.2	−118.8
378,000	378,194.4	+194.4
	377,564.4	−435.6
	431,336.4	−633.6
432,000	432,000.0	0.0
	432,313.2	+313.2
	486,432.0	+432.0
486,000	485,802.0	−198.0
	486,115.2	+115.2
	540,234.0	+234.0
540,000	540,550.8	+550.8
	539,604.0	−396.0
	593,722.8	−277.2
594,000	594,036.0	+36.0
	594,352.8	+352.8
	648,471.6	+471.6
648,000	647,524.8	−475.2
	648,154.8	+154.8
	701,960.4	−39.6
702,000	702,273.6	+273.6
	701,643.6	−356.4
	755,445.6	−554.4
756,000	756,075.6	+75.6
	756,392.4	+392.4
	810,194.4	+194.4
810,000	809,881.2	−118.8
	809,564.4	−435.6
	864,630.0	+630.0
864,000	864,313.2	+313.2
	863,366.4	−633.6
	917,802.0	−198.0
918,000	917,485.2	−514.8
	918,115.2	+115.2

Table 13. *Cont.*

Rotational Angular Displacement /″	Test Angular Displacement /″	Absolute Error /″
	972,550.8	+550.8
972,000	971,604.0	−396.0
	972,234.0	+234.0
	1,025,406.0	−594.0
1,026,000	1,026,352.8	+352.8
	1,026,036.0	+36.0
	1,079,524.8	−475.2
1,080,000	1,080,154.8	+154.8
	1,080,471.6	+471.6
	1,134,273.6	+273.6
1,134,000	1,133,643.6	−356.4
	1,134,590.4	+590.4
	1,188,075.6	+75.6
1,188,000	11,88,392.4	+392.4
	1,187,445.6	−554.4
	1,242,511.2	+511.2
1,242,000	1,241,881.2	−188.8
	1,241,564.4	−435.6
	1,296,313.2	+313.2
1,296,000	1,295,366.4	−633.6
	1,296,630.0	+630.0

5. Conclusions

The assembly design proposed in this study addresses the limitations of conventional integration methods between CSRs and encoders in industrial equipment, significantly enhancing system reliability and stability. Static and dynamic finite element analyses were conducted for the hollow-type assembly, followed by the construction of a dedicated test platform. A novel test method based on the R-axis rotary platform was developed to evaluate assembly performance. These findings indicate that the proposed hollow integrated assembly design effectively addresses the challenges of integrating CSRs and encoders in industrial equipment, significantly enhancing system reliability and stability. The main contributions and conclusions are as follows:

1. A complete scheme for the hollow-type assembly was designed. The transmission module includes a design for a smooth shaft drive and a sleeve-type coupling. The clamping module incorporates both hollow and flange-type connecting frames. The protective module comprises a small-aperture adapter plate and a guide-sleeve cover. The instrumentation module includes the selection of a through-hole slip ring and a photoelectric encoder, with the final slip ring chosen as the Senring H0835-0605TC model. The reliability of the assembly was ensured through torsional theory analysis and simulation.
2. Static analysis determined the optimal assembly angle to be 0°, yielding a maximum stress of 0.913 MPa and a maximum displacement of 0.0316 μm—both well below the allowable design thresholds, indicating ample safety margin. Modal analysis revealed that the hollow-type frame's natural frequency ranges from 585.24 Hz to 4431.20 Hz, with the first mode at 585.24 Hz, significantly exceeding the 400 Hz requirement. Comparatively, the flange-type frame exhibited approximately 30% lower dynamic stability.
3. A dedicated performance testing system was developed based on the R-axis rotary platform, offering an angular resolution of 0.001°, a rotational speed range of

0–100 rpm, and a data acquisition frequency of 10 kHz—providing a robust foundation for performance evaluation. In terms of electrical performance, contact resistance remained between 36.23 and 38.76 mΩ, with fluctuation under 10 mΩ, fully meeting design specifications. In terms of mechanical performance, the custom sleeve-type coupling reduced angular displacement error by approximately 40%, while the hollow-type frame effectively decreased vibration response by 35%. The angular repeatability reached 499.8″ and the accuracy 705.6″—both superior to the technical requirements.

Overall, the hollow-type assembly demonstrated comprehensive compliance with or exceeded all performance benchmarks. The innovative sleeve-type coupling notably enhanced transmission accuracy, while the hollow-type connecting frame exhibited excellent dynamic characteristics. The complete system meets industrial-grade reliability standards. This research successfully resolves the technical challenge of integrating slip rings with encoders, offering an effective solution for improving performance in related industrial applications. However, there are limitations to this study. The performance testing was conducted under specific environmental conditions; the results may vary under different conditions. Future research will explore the performance of the assembly under a wider range of environmental conditions, such as temperature and humidity variations. Additionally, the long-term durability and wear characteristics of the assembly require further investigation to ensure sustained performance in industrial applications.

Author Contributions: Conceptualization, Z.Q. and N.L.; methodology, C.H.; software, G.T.; validation, Z.Q., N.L., and H.W.; formal analysis, J.L.; investigation, J.L.; resources, J.L.; data curation, J.L.; writing—original draft preparation, C.H.; writing—review and editing, N.L.; visualization, G.T.; supervision, H.W.; project administration, J.L.; funding acquisition, J.L. All authors have read and agreed to the published version of the manuscript.

Funding: This research was funded by Shanghai Science and Technology Project, grant number 23DZ2229032; Science and Technology Development Plan Project of Jilin Province, grant number 20220201036GX.

Data Availability Statement: The data that support the findings of this study are available from the corresponding author upon reasonable request.

Acknowledgments: The authors are grateful to the referees for their constructive comments and suggestions, which have improved the manuscript.

Conflicts of Interest: Author Haihong Wu was employed by the company China Shipbuilding Jiujiang Marine Equipment (Group) Co., Ltd. The remaining authors declare that the research was conducted in the absence of any commercial or financial relationships that could be construed as a potential conflict of interest.

Abbreviations

The following abbreviations are used in this manuscript:

CSR Conductive slip ring

References

1. Dong, T.Y.; Li, L.; Wei, H.X. Introduction to the formulation of CB 20363-2018 Code for Conductive slip Rings for Shipborne Radar. *Shipbuild. Stand. Qual.* **2019**, *2019*, 25–27+20.
2. Zhang, Q.; Zhang, K.M.; Liu, J.K. Overview of Research and Development on Space Slip Rings. *J. Mech. Eng.* **2022**, *58*, 334–348.
3. Liu, B.; Lu, X. Interpolation error analysis of photoelectric encoder based on improved genetic algorithm. *J. Electron. Meas. Instrum.* **2019**, *33*, 15–20.

4. Niu, G.; Wu, H.; Qian, Z.; Liu, C.; Ma, Z. Research on the prediction model for the wear of bundle brush conductive slip ring in spacecraft. In Proceedings of the SPIE 12801, Ninth International Conference on Mechanical Engineering, Materials, and Automation Technology (MMEAT 2023), 12801, Dalian, China, 9–11 June 2023; pp. 549–564.
5. Zhang, S.M.; Qiang, Q.; Liu, L.Y.; Jie, X. Effect of Ring Hardness on Friction and Wear Properties of Gold-base Alloy Slip Rings. *Tribology* **2024**, *44*, 358–367.
6. Li, J.Y.; Li, J.; Wang, X.P.; Tian, G.; Fan, J. Machine vision-based method for measuring and controlling the angle of conductive slip ring brushes. *Micromachines* **2022**, *13*, 447. [CrossRef] [PubMed]
7. Chen, X.; Wang, Y.; Sheng, Y.; Yu, C.; Yang, X.; Xi, J. Vision-Aided Brush Alignment Assembly System for Precision Conductive Slip Rings. *Machines* **2022**, *10*, 393. [CrossRef]
8. Jia, Q.J.; Yao, P. Frictional Torque Analysis of Space Conductive Slip Ring under Vacuum and High and Low Temperature Environment. *Lubr. Eng.* **2020**, *45*, 123–127.
9. Yang, J.Y.; Liu, M.H.; Song, X.L.; Lei, J.J. Numerical study on heat transfer characteristics of brush seal. *J. Mech. Electr. Eng.* **2021**, *38*, 1230–1237.
10. Jiang, K.; Li, J.W.; Gao, F. Structure Design of Conductive Slip Ring for Underwater Micro-submersible Submarine. *Mach. Build. Autom.* **2020**, *49*, 28–30.
11. Li, W.G.; Fu, H.B.; Zhang, F.F. Research on a new type of ultra-small conductive slip ring. *Technol. Innov. Appl.* **2022**, *12*, 57–59+64.
12. Li, W.G.; Fu, H.B.; Zhang, F.F. The utility model relates to a long life conductive slip ring which is convenient for center of mass trimming. *Technol. Innov. Appl.* **2020**, *2022*, 92–93.
13. Liu, M.; Meng, L.X.; Zhang, L.Z.; Chen, L.B.; Zhang, Z.W. Study on fatigue characteristics of 'goose-neck' type limited angle Conductive Slip Ring. *J. Chang. Univ. Sci. Technol. (Nat. Sci. Ed.)* **2021**, *44*, 44–50.
14. Feng, T.; Chen, W.L.; Qiu, J.J.; Hao, S.H. A new kind of absolute magnetic encoder. *Sensors* **2021**, *21*, 3095. [CrossRef]
15. Wang, S.D.; Zhu, W.L.; Shen, Y.J.; Ren, J.; Gu, H.R.; Wei, X.Y. Temperature compensation for MEMS resonant accelerometer based on genetic algorithm optimized backpropagation neural network. *Sens. Actuators A Phys.* **2020**, *316*, 112393. [CrossRef]
16. Han, S.; Ahn, Y.; Kang, K.; Shin, J.W. Short-segment speaker verification using ECAPA-TDNN with multi-resolution encoder. In Proceedings of the CASSP 2023–2023 IEEE International Conference on Acoustics, Speech and Signal Processing (ICASSP), Rhodes Island, Greece, 4–10 June 2023; pp. 1–5.
17. Sun, Z.; Sumsion, A.W.; Torrie, S.A.; Lee, D.J. Learning facial motion representation with a lightweight encoder for identity verification. *Electronics* **2022**, *11*, 1946. [CrossRef]
18. Zhang, B.; Li, Y.; Chen, X.L. Design and development of high precision magnetic encoder for servo positioning experiment system. *Exp. Technol. Manag.* **2021**, *38*, 183–192.
19. Wang, C.F.; Xue, C.R.; Huang, H.Y. Improved design of installation structure of rotary encoder for shotcreting robot. *Coal Mine Mach.* **2023**, *44*, 129–131.
20. Huang, L.X.; Huang, J.Y.; Huang, L.J. Design of encoder based on giant magnetoresistance sensor. *Appl. IC* **2023**, *40*, 11–13.
21. Yin, Q.Y.; Wu, R.P.; Chen, W.W. Survival analysis algorithm based on multi-omics data and variational sparse autoencoder. *Appl. Res. Comput.* **2023**, *40*, 771–775.
22. Sheng, D.D. *Design and Error Compensation of Magnetic Encoder*; Northeast Electric Power University: Jilin, China, 2023.
23. Zhao, R.F. *Design and Realization of High-Resolution and High-Accuracy Magnetic Encoder Based on TMR*; Hangzhou Dianzi University: Hangzhou, China, 2021.
24. Ludois, D.C.; Frankforter, K. A rotating double layer capacitive slip ring concept for power & heat transfer in machines using an ionic conducting working fluid. In Proceedings of the 2020 IEEE Energy Conversion Congress and Exposition (ECCE), Detroit, MI, USA, 11–15 October 2020; pp. 4238–4245.
25. Tu, W.Y.; Qian, J.; Xu, X.D. Assembly analysis of the axial system of large high-precision optical shaft encoder. *Manuf. Technol. Mach. Tool* **2011**, *2011*, 46–48.
26. Wang, X.Y. Connection between motors and encoders as well as its assembly points. *Electr. Mach. Technol.* **2020**, *2020*, 57–59.
27. Li, G.J. Mechanical and finite element analysis of membrane coupling. *Heavy Mach.* **2022**, *2022*, 76–80.
28. Xue, R.B. Between shaft and shaft coupling research in production and improve the design. *Friend Sci. Amat.* **2013**, *2013*, 35–37.
29. Ma, J.; Meng, G. Structural design of interference fit coupling. *Intern. Combust. Engine Parts* **2019**, *2019*, 122–123.
30. Zhao, Z.D.; Cun, W.Y.; Qian, J.; Zhao, X.S.; Shu, Y.; Chen, G. Simulation analysis and test verification of aircraft pipeline fatigue performance. *Noise Vib. Control* **2023**, *43*, 239–244+279.
31. Zhang, T.Y. *Assembly Accuracy Prediction and Control for Precision Mechanical System*; Beijing Institute of Technology: Beijing, China, 2016.

32. Zhang, B.Y. *Development of an Angle Encoder Calibration Device for High and Low Temperature Environments*; China Jiliang University: Hangzhou, China, 2019.
33. *ISO 9283-1998*; Manipulating Industrial Robots: Performance Criteria and Related Test Methods. International Organization for Standardization: Geneva, Switzerland, 1998.

Disclaimer/Publisher's Note: The statements, opinions and data contained in all publications are solely those of the individual author(s) and contributor(s) and not of MDPI and/or the editor(s). MDPI and/or the editor(s) disclaim responsibility for any injury to people or property resulting from any ideas, methods, instructions or products referred to in the content.